Dilena, M., Dell'Oste, M. F., Fernández-Sáez, J., Morassi, A. & Zaera, R. (2019, diciembre). Identification of general added mass distribution in nanorods from two-spectra finite data. Mechanical Systems and Signal Processing, 134, 106286.

DOI: 10.1016/j.ymssp.2019.106286

Identification of general added mass distribution in nanorods from two-spectra finite data

M. Dilena[a], M. Fedele Dell'Oste[a], J. Fernández-Sáez[b], A. Morassi[a], R. Zaera[b]

[a] *Polytechnic Department of Engineering and Architecture, University of Udine, via Cotonificio 114, 33100 Udine, Italy*
[b] *Department of Continuum Mechanics and Structural Analysis, Universidad Carlos III de Madrid, Av. de la Universidad 30, 28911 Leganés, Madrid, Spain*

Abstract

Nanomechanical resonators consisting in one-dimensional vibrating structures have remarkable performance in detecting small adherent masses. The mass sensing principle is based on the use of the resonant frequency shifts caused by unknown attached masses. In spite of its importance in applications, few studies are available on this inverse problem. Dilena et al. (2019) presented a method for reconstructing a small mass distribution by using the first N resonant frequencies of the free axial vibration of a nanorod under clamped end conditions. In order to avoid trivial non-uniqueness when spectral data belonging to a single spectrum are used, the mass variation was supposed to be supported in half of the axis interval. In this paper, we remove this a priori assumption on the mass support, and we show how to extend the method to reconstruct a *general* mass distribution by adding to the input data the first N lower eigenvalues of the nanorod under clamped-free end conditions. The nanobeam is modelled using the modified strain gradient theory to account for the microstructure and size effects. The reconstruction is based on an iterative procedure which takes advantage of the closed-form solution available when the mass change is small, and turns out to be convergent under this assumption. The results of an extended series of numerical simulations support the theoretical results.

Keywords: Strain gradient theory, nanosensors, nanorods, mass identification,

inverse problems, axial vibration.

1. Introduction

Nanosensors are gathering attention in the last decade due to the necessity of measuring physical and chemical properties in industrial or biological systems at the sub-micron scale [1, 2]. One of the most representative examples of down-scaling in sensoring systems is the nanomechanical resonator, which typically consists in a one-dimensional vibrating structure with remarkable performance in detecting small adherent masses [3]. The *mass sensing principle* for these systems is based on using the resonant frequency shifts caused by unknown additional masses attached on the surface of the sensor as data for the reconstruction of the mass variation.

In spite of its importance in applications, few results are available on this inverse problem. Actually, there are studies, although not numerous, on the identification of small concentrated masses in classical beams and rectangular plates, see, for example, [4] and [5]. For the sake of completeness, we also mention the recent contributions [6], [7] in which the identification of an open crack in a vibrating rod or beam, respectively, is reduced to the identification of a point mass placed at the cracked cross-section. Sufficient conditions for the uniqueness of the solution to this inverse problem were established in [6], [7] by using minimal resonant frequency data, without any a priori assumption on the smallness of the attached mass and for beams with smooth variable profile.

It should be noticed that the above works are based on classical elasticity principles. Therefore, the corresponding mechanical models are not able to take into account those microstructure and scale effects that are relevant in predicting the dynamical response of nanostructures, commonly used as mass sensors, as it has been shown through experimental results by different authors, see, for

instance, [8, 9, 10, 11].

Among the generalized continuum approaches, we cite here three main groups: the microcontinuum theory [12] including micropolar, microstretch and micromorphic ($3M$) theories (Cosserat micropolar elasticity [13] should be considered in this category as the simplest formulation among ($3M$) theories). Inside this group of theories, it is worth to cite the recent papers by Shaat [14] and Ansari et al. [15]. The other two groups are the different versions of nonlocal continuum mechanics theories and the strain gradient elasticity family. In the sequel, some more details of the approaches belonging in this two last groups are given, in view of their wide use in the last fifteen years to address problems related to the mechanical behaviour of nanostructures.

The origin of nonlocal continuum mechanics theories can be found in the works by Kroner [16], Krumhansl [17], and Kunin [18]. They were later simplified by Eringen and coworkers ([19, 20, 21, 22]), and formulated originally in integral form for linear homogeneous isotropic elastic materials. In this model, called strain-driven formulation of the nonlocal elasticity, the stress at a point of a solid depends on the strain at all points of the domain. This dependence is represented by a convolution integral with a smoothing kernel. Eringen [22] showed that, for a specific class of kernel functions, the nonlocal integral constitutive equation can be transformed into a differential form, which fairly simplify the analysis. Exploiting this simplification, the differential approach has been widely used to analyze the mechanical behaviour of nanostructures, see the recent reviews by Eltaher et al. [23], Rafii-Tabar et al. [24], and Thai et al. [25] which summarises the huge number of publications on the subject since the pioneer work of Peddieson et al. [26]. Nevertheless, Romano et al. [27] clearly showed that, in the majorities of the cases, the fully nonlocal elasticity theory (strain-driven) leads to problems that have to be considered as ill-posed, with no solution in general. Therefore, this model is not feasible to assess scale effects in nanostructures. To overcome these drawbacks, Romano et al. [28]

proposed an alternative formulation of the pure nonlocal strain-driven elastic model. The new nonlocal model, called stress-driven, considers that elastic strain at a point is represented by a convolution integral of the stress field and a smoothing kernel. The approach leads to well-posed problems when it is applied to several kinds of nanostructures ([29, 30, 31, 32, 33]). The ill-posedness of the pure strain-driven nonlocal problem can also be removed using the two-phase local/nonlocal strain-driven constitutive model, which was first proposed by Eringen [19, 34] and later applied by different authors ([35], [36], [37], [38], and [39]) to address several problems related to the statics and dynamics of nanostructures. Moreover, the two-phase local/nonlocal stress-driven constitutive model have been recently developed [40, 41].

Other very popular approaches to analyse the mechanical behaviour of nanostructures are the strain gradient elasticity family including the couple stress theory [42, 43, 44], the first and second strain gradient theories of Mindlin [45, 46], the modified couple stress theory [47] and the modified strain gradient theory [9]. The last one [9] is a simplification of previous formulations due to Mindlin [46] and Fleck and Hutchinson [48], and requires new additional equilibrium equations to govern the behavior of higher-order stresses. Only three non-classical constants for isotropic linear elastic materials are needed in this theory. Regarding the use of this theory to model the mechanical behaviour of nanobeams it is necessary to mention the works by Kong et al. [49] who studied the static and dynamic bending behavior of Euler-Bernoulli beams, and of Wang et al. [50] dealing with the problem of Timoshenko beams. Further Akgoz and Civalek [51, 52] derived analytical solutions for the buckling problem of axially loaded nano-sized beams. Besides the previous analytical works, and in the context of the modified strain gradient theory, Kahrobaiyan et al. [53] and Zhang et al. [54] developed an Euler-Bernoulli and Timoshenko finite beam elements, respectively for the study of static bending, free vibration and buckling behavior of microbeams. The interested reader can see the very re-

cent review by Thai et al. [25] for relevant applications to the analysis of the mechanical response of different kinds of nanostructures. Moreover, it is worth to note that the modified strain gradient formulation is more general than the couple stress theory. In fact, this last theory can be considered a special case of the proposed one by Lam et al. [9]. The classical continuum theory can be also recovered cancelling the scale parameters present in the strain gradient theory.

Lim et al. [55] combine in a unique theory both the pure nonlocal elasticity theory of Eringen and the strain gradient elasticity. The resulting theory, called nonlocal strain gradient theory, contains two non-classical material parameters, the nonlocal parameter and the gradient coefficient. Since then, a large number of papers have been published applying this theory to nanostructures. Here we only quote a few examples ([56, 57, 58, 59, 60, 61, 62, 63]). The application of the theory to bounded domains implies the need to fulfil both classical and non-classical (higher-order) boundary conditions, as well as the inherent boundary conditions imposed by the nonlocal constitutive equations (constitutive boundary conditions). However, the above works did not consider all the boundary conditions (classical, non-classical and constitutive) in the analysis. In fact, Zaera et al. [64] shown that, in general, is not possible to accomplish simultaneously the boundary conditions, which are all mandatory in the framework of the nonlocal strain gradient elasticity, and therefore, the problems formulated through this theory have no solution.

Finally, we refer here some approaches combining the strain gradient elasticity and the surface elasticity, proposed by Gurtin and Murdoch ([65, 66]), in order to explain the size effects present in nanostructures. In this respect we quote the recent papers by Mirkalantari et al. [67] and Fu et al. [68], among others.

The modified strain gradient theory seems to be an attractive formulation accounting for the scale effect present in nanostructures. The size dependence of deformation behavior in the micron scale observed in metals [48] and poly-

mers [9], could be explained by the strain gradient-based constitutive equations considered in this formulation. Moreover, within the modified strain gradient theory proposed in [9], the identification of a single point mass was previously considered in [69] and [70] for nanobeams under longitudinal or bending vibrations, respectively, and in [71] for the case of rectangular simply-supported Kirchhoff-Love nanoplates.

Although the majority of the research efforts have been focused until now on the identification of concentrated masses attached to a baseline nanosystem, a distributed mass representing the adsorbed analyte seems to be more realistic in several applications. Hanay et al. [72] proposed an *inertial imaging* method to determine the first N moments of the unknown mass distribution in terms of the shifts in the first N resonant frequencies, under the assumption of small global mass change. The analysis is applied to the transverse vibration of a clamped-clamped nanobeam, but, however, the formulation relies on the classical elasticity theory. Using the modified strain gradient framework [9] to account for size effects, the inverse problem of determining the mass distribution of a nanorod from the knowledge of the first N resonant frequencies of the free axial vibration under clamped ends was originally addressed in [73]. Let us recall that the free axial vibration of a nanorod is governed by a differential operator with fourth order leading term, instead of a second-order operator, as it occurs for classical beams. Assuming that the mass coefficient is *a priori known on half* of the nanorod, and that the added mass is a *small perturbation* of the total mass of the nanosensor, the reconstruction procedure produces an approximation of the unknown mass density as a generalized Fourier partial sum of order N, whose coefficients are calculated from the first N eigenvalues. The approach corresponds to a mixed formulation of the inverse eigenvalue problem with finite data, see, for example, the interesting paper by Barnes [74] and the introductory section in [73] for an overview of the main mathematical features of this class of problems.

In this paper we continue the line of research initiated in [73] and we consider the more general inverse problem of determining a mass variation *not necessarily supported* in half of the nanorod interval axis. More precisely, we propose a reconstruction method based on the knowledge of a finite number of lower resonant frequencies belonging to two spectra corresponding to clamped-clamped and clamped-free end conditions. It can be shown that the recourse to a second partial spectrum is necessary in order to avoid trivial non uniqueness of the solution to the inverse problem. Roughly speaking, the information coming from one spectrum was replaced in [73] by the *a priori* knowledge of the mass distribution on one half of the nanobeam axis. Under the assumption that the added mass is small with respect to the global mass of the referential nanorod, we show that the first-order frequency shifts can be used to determine a set of generalized Fourier coefficients of the unknown mass variation on a suitable set of functions. In case of uniform unperturbed nanorod, the procedure allows for a closed form solution of the linearized inverse problem. An iterative reconstruction procedure based on first-order Taylor approximation of the eigenvalues is proposed and implemented to solve the inverse problem. The reconstruction procedure is shown to be convergent, provided that the eigenvalues of the unperturbed nanobeam are close enough to the corresponding target eigenvalues.

The method has been tested on a large class of mass variations, including smooth (e.g., continuous) and discontinuous added mass distributions. Numerical reconstruction shows good accuracy in the smooth cases. Precise pointwise approximations are obtained even when only the first $N = 9, 12$ eigenfrequencies of both spectra are used in identification. It should be noticed that the high quality of the reconstruction obtained in these cases is rather unexpected, since the general mathematical results available in the literature for fourth-order Euler-Bernoulli's-like differential operators are more pessimistic, see, among other contributions, [75], [76], [77]. The reconstruction of discontinuous coefficients turns out to be less accurate, and the identified mass coefficient exhibits appre-

ciable oscillations near the jumps.

The plan of the paper is as follows. The formulation of the mass identification problem is presented in Section 2. Section 3 describes the reconstruction method. The evaluation of the performance of the reconstruction method is illustrated in Section 4. This section includes results corresponding to both continuous (Section 4.2) and discontinuous mass distributions (Section 4.3). The robustness of the proposed methodology is tested by using noisy resonant frequencies belonging to the two spectra (Section 4.4). Finally, some concluding remarks are collected in Section 5.

2. Formulation of the inverse problem

The spatial variation of the infinitesimal free axial vibration at radian frequency $\sqrt{\lambda}$ of the *unperturbed* uniform nanorod, of length L and under clamped end conditions, is governed within the modified strain gradient theory by the following eigenvalue problem [78, 69]

$$\begin{cases} bv^{IV} - av'' = \lambda \rho_0 v, \quad x \in (0, L), & (1) \\ v(0) = 0, \ v''(0) = 0, & (2) \\ v(L) = 0, \ v''(L) = 0, & (3) \end{cases}$$

where λ is the eigenvalue and $v = v(x)$ is the corresponding eigenfunction. The coefficient $\rho_0 = const.$, $\rho_0 > 0$, is the unperturbed mass density per unit length. The coefficient $a = const.$, $a > 0$, is the axial stiffness of the nanorod, and it can be expressed as $a = EA$, with E, $E > 0$, being the Young's modulus, and A being a geometrical parameter that may be set to correspond with the cross-sectional area of the nanorod [78]. The coefficient $b = const.$, $b > 0$, is determined as

$$b = GA\left(2l_0^2 + \frac{4}{5}l_1^2\right), \quad (4)$$

where $G = E/(2(1+\nu))$ is the shear modulus defined in terms of E and of Poisson ratio ν, $\nu > 0$, and $l_0 > 0$, $l_1 > 0$ are length scale parameters [9, 78, 69].

The eigenpairs $\{\lambda_n^C, v_n^C(x)\}_{n=1}^{\infty}$ of (1)–(3) are

$$\lambda_n^C = \left(\frac{n\pi}{L}\right)^2 \left[\frac{1}{\rho_0}\left(a + b\left(\frac{n\pi}{L}\right)^2\right)\right], \tag{5}$$

$$v_n^C(x) = \sqrt{\frac{2}{\rho_0 L}} \sin\left(\frac{n\pi x}{L}\right), \tag{6}$$

where the eigenfunctions are mass-normalized such that

$$\int_0^L \rho_0 (v_n^C(x))^2 = 1, \quad n \geq 1. \tag{7}$$

If in (1)–(3) the boundary conditions (3) are replaced by

$$v'(L) = 0, \quad v'''(L) = 0, \tag{8}$$

then the nanorod is said to be under *clamped-free* end conditions, and the eigenvalues of (1), (2), (8) are

$$\lambda_n^F = \left(\frac{(2n-1)\pi}{2L}\right)^2 \left[\frac{1}{\rho_0}\left(a + b\left(\frac{(2n-1)\pi}{2L}\right)^2\right)\right], \tag{9}$$

$$v_n^F(x) = \sqrt{\frac{2}{\rho_0 L}} \sin\left(\frac{(2n-1)\pi x}{2L}\right), \tag{10}$$

with $\int_0^L \rho_0 (v_n^F(x))^2 = 1$ for every $\quad n \geq 1$.

Let us assume that the mass density changes, and denote by

$$\rho(x) = \rho_0 + r_\epsilon(x), \quad x \in [0, L], \tag{11}$$

the mass density per unit length of the *perturbed* nanorod. The mass change r_ϵ is such that

$$\left(\frac{1}{L}\int_0^L (r_\epsilon(x))^2 dx\right)^{\frac{1}{2}} = \epsilon\rho_0, \tag{12}$$

$$r_\epsilon(x) \in L^\infty([0, L]), \tag{13}$$

$$0 < \rho^- \leq \rho(x) \leq \rho^+, \quad x \in [0, L], \tag{14}$$

where ϵ, $0 < \epsilon \leq \widehat{\epsilon}_\rho$, for a given small number $\widehat{\epsilon}_\rho$, and ρ^-, ρ^+ are given constants (with $\rho^+ \geq \rho_0 + \|r_\epsilon\|_\infty$) independent of ϵ. Hereinafter, $L^\infty([0,L])$ is the space of (Lebesgue measurable) functions $f : [0,L] \to \mathbb{R}$ such that $\|f\|_\infty = ess\ sup_{x\in[0,L]}|f(x)| < \infty$ almost everywhere in $[0,L]$. Moreover, $L^2(0,L)$ is the space of (Lebesgue measurable) functions $f : [0,L] \to \mathbb{R}$ such that $\|f\|_2 = \left(\int_0^L f^2(x)dx\right)^{1/2} < \infty$.

Let us denote by $\{\lambda_n^C(\rho), v_n^C(x;\rho)\}_{n=1}^\infty$, $\{\lambda_n^F(\rho), v_n^F(x;\rho)\}_{n=1}^\infty$ the eigenpairs of the problems (1)–(3) and (1), (2), (8), respectively, when ρ_0 is replaced by $\rho(x)$.

In this paper we wish to construct an approximation to $\rho(x)$ (or, equivalently, to $r_\epsilon(x)$) using a finite amount of spectral data belonging to the clamped-clamped and clamped-free spectra, namely, the set

$$\{\lambda_n^C(\rho)\}_{n=1}^N \bigcup \{\lambda_m^F(\rho)\}_{m=1}^M, \tag{15}$$

where N, M are given integers.

Our main result is the development of a reconstruction procedure that, under suitable assumptions on the smallness of the mass variation and on the smallness of the eigenvalues shifts between unperturbed and perturbed eigenvalues, converges to a mass density function which has the wished spectral properties.

3. The reconstruction method

Our reconstruction method is obtained as a generalization of the method presented in [73], and it is based on a sequence of linearizations of the inverse problem with finite data. We first present the linearization in a neighborhood of the unperturbed nanorod. Next, we shall introduce the iterative version of the identification procedure.

A key mathematical tool in our analysis is the explicit expression of the first order change with respect to the smallness parameter ϵ of an eigenvalue of the

nanorod. With reference to the initial uniform nanorod, we have

$$\delta\lambda_n^C \equiv 1 - \frac{\lambda_n^C(\rho)}{\lambda_n^C} = \int_0^L r_\epsilon(x)\Phi_n^C(x)dx, \tag{16}$$

$$\delta\lambda_m^F \equiv 1 - \frac{\lambda_m^F(\rho)}{\lambda_m^F} = \int_0^L r_\epsilon(x)\Phi_m^F(x)dx, \tag{17}$$

where $\Phi_n^C(x) \equiv (v_n^C(x))^2$, $\Phi_m^F(x) \equiv (v_m^F(x))^2$, $n = 1, \ldots, N$, $m = 1, \ldots, M$. This result has been proved in [73] for clamped end conditions and can be generalized to clamped-free end conditions. A simple calculation shows that (up to an inessential multiplicative constant)

$$\{\Phi_n^C(x), \Phi_m^F(x)\}_{n,m=1}^{\infty} = \{1 - \cos(k\pi x/L)\}_{k=1}^{\infty}, \tag{18}$$

which is a basis of $L^2(0, L)$. This property enables us to introduce the representation

$$r_\epsilon(x) = \sum_{k=1}^{\infty} \beta_k^C \Phi_k^C(x) + \beta_k^F \Phi_k^F(x), \tag{19}$$

where the coefficients $\{\beta_k^C, \beta_k^F\}_{k=1}^{\infty}$ play the role of Generalized Fourier Coefficients of the mass variation $r_\epsilon(x)$. Replacing the above series expansion of $r_\epsilon(x)$ in (16) and (17), and taking the finite approximation of order $(N + M)$ of $r_\epsilon(x)$ in (19), we obtain the $(N + M) \times (N + M)$ linear system

$$\mathbf{A}\boldsymbol{\beta} = \boldsymbol{\delta\lambda}, \tag{20}$$

or, more explicitly,

$$\begin{pmatrix} A_{11}^{C-C} & \cdots & A_{1N}^{C-C} & A_{11}^{C-F} & \cdots & A_{1M}^{C-F} \\ \cdots & & \cdots & \cdots & & \cdots \\ A_{N1}^{C-C} & \cdots & A_{NN}^{C-C} & A_{N1}^{C-F} & \cdots & A_{NM}^{C-F} \\ A_{11}^{F-C} & \cdots & A_{1N}^{F-C} & A_{11}^{F-F} & \cdots & A_{1M}^{F-F} \\ \cdots & & \cdots & \cdots & & \cdots \\ A_{M1}^{F-C} & \cdots & A_{MN}^{F-C} & A_{M1}^{F-F} & \cdots & A_{MM}^{F-F} \end{pmatrix} \begin{pmatrix} \beta_1^C \\ \cdots \\ \beta_N^C \\ \beta_1^F \\ \cdots \\ \beta_M^F \end{pmatrix} = \begin{pmatrix} \delta\lambda_1^C \\ \cdots \\ \delta\lambda_N^C \\ \delta\lambda_1^F \\ \cdots \\ \delta\lambda_M^F \end{pmatrix}, \tag{21}$$

with

$$A_{nk}^{C-C} = \int_0^L \Phi_n^C(x)\Phi_k^C(x)dx, \quad n,k = 1,\cdots N, \tag{22}$$

$$A_{nk}^{C-F} = \int_0^L \Phi_n^C(x)\Phi_k^F(x)dx, \quad n = 1,\cdots N,\ k = 1,\cdots M, \tag{23}$$

$$A_{mk}^{F-C} = \int_0^L \Phi_k^C(x)\Phi_m^F(x)dx, \quad k = 1,\cdots N,\ m = 1,\cdots,M, \tag{24}$$

$$A_{mk}^{F-F} = \int_0^L \Phi_m^F(x)\Phi_k^F(x)dx, \quad m,k = 1,\cdots,M. \tag{25}$$

A direct calculation based on the explicit expressions of the eigenfunctions (6) and (10), shows that the entries of the matrix $\mathbf{A}$ are given by

$$A_{mn} = \frac{1}{\rho_0^2 L} \text{ for } m \neq n, \quad A_{nn} = \frac{3}{2\rho_0^2 L}, \tag{26}$$

$m,n = 1,\cdots,M+N$, and

$$\det(\mathbf{A}) = (2M+2N+1)\left(\frac{1}{2\rho_0^2 L}\right)^{M+N}, \tag{27}$$

$$(\mathbf{A})_{mn}^{-1} = -(2\rho_0^2 L)\frac{2}{2M+2N+1} \text{ for } m \neq n, \quad (\mathbf{A})_{nn}^{-1} = (2\rho_0^2 L)\frac{2M+2N-1}{2M+2N+1}, \tag{28}$$

$m,n = 1,\cdots,M+N$. Therefore, the unknown vector $\boldsymbol{\beta}$ in (21) has the following expression

$$\beta_n^C = \frac{2\rho_0^2 L}{2M+2N+1}\left((2M+2N-1)\delta\lambda_n^C - 2\left(\sum_{k=1,k\neq n}^{N}\delta\lambda_k^C + \sum_{j=1}^{M}\delta\lambda_j^F\right)\right), \tag{29}$$

$$\beta_m^F = \frac{2\rho_0^2 L}{2M+2N+1}\left((2M+2N-1)\delta\lambda_m^F - 2\left(\sum_{k=1,k\neq m}^{M}\delta\lambda_k^F + \sum_{j=1}^{N}\delta\lambda_j^C\right)\right) \tag{30}$$

$n = 1, ..., N$, $m = 1, ..., M$, and the first-order mass variation can be obtained
205 by means of equation (19) (truncated series).

The accuracy in the determination of $r_\epsilon(x)$ can be improved by iterating the above procedure as follows. Let us denote by $\{\lambda_n^{C(exp)}\}_{n=1}^N$, $\{\lambda_m^{F(exp)}\}_{m=1}^M$ the measured (or *target*) values of the eigenvalues $\{\lambda_n^C(\rho)\}_{n=1}^N$, $\{\lambda_m^F(\rho)\}_{m=1}^M$ of the perturbed nanorod with mass density $\rho(x) = \rho_0 + r_\epsilon(x)$. The function $\rho(x)$ is determined in $[0, L]$ by the iterative process

$$\rho^{(j+1)}(x) = \rho^{(j)}(x) + r^{(j)}(x), \quad j \geq 0, \tag{31}$$

with $\rho^{(0)}(x) \equiv \rho_0$. Note that the subscript ϵ has been omitted to simplify the notation. The increment

$$r^{(j)}(x) = \sum_{k=1}^{N} \beta_k^{C(j)} \Phi_k^{C(j)}(x) + \sum_{k=1}^{M} \beta_k^{F(j)} \Phi_k^{F(j)}(x) \tag{32}$$

is evaluated by solving the $(N + M) \times (N + M)$ linear system

$$\boldsymbol{A}^{(j)} \boldsymbol{\beta}^{(j)} = \boldsymbol{\delta\lambda}^{(j)}, \tag{33}$$

in which $\boldsymbol{\delta\lambda}^{(j)} = (\delta\lambda_1^{C(j)}, \cdots, \delta\lambda_N^{C(j)}, \delta\lambda_1^{F(j)}, \cdots, \delta\lambda_M^{C(j)})$, with

$$\delta\lambda_n^{C(j)} \equiv 1 - \frac{\lambda_n^{C(exp)}}{\lambda_n^C(\rho^{(j)})}, \quad n = 1, \cdots, N, \tag{34}$$

$$\delta\lambda_m^{F(j)} \equiv 1 - \frac{\lambda_m^{F(exp)}}{\lambda_m^F(\rho^{(j)})}, \quad m = 1, \cdots, M. \tag{35}$$

The entries of the matrix $\mathbf{A}^{(j)}$ are as in (22)–(25), with the functions $\Phi_n^C(x)$, $\Phi_m^F(x)$ replaced by $\Phi_n^{C(j)}(x) = (v_n^C(x; \rho^{(j)}))^2$, $\Phi_m^{F(j)}(x) = (v_m^F(x; \rho^{(j)}))^2$, $n = 1, \cdots, N$, $m = 1, \cdots, M$. Here, $\{\lambda_n^C(\rho^{(j)}), v_n^C(x; \rho^{(j)})\}$, $\{\lambda_m^F(\rho^{(j)}), v_m^F(x; \rho^{(j)})\}$ are the nth and mth (mass normalized) eigenpairs of the clamped and clamped-free nanobeam with mass density $\rho^{(j)}(x)$, respectively. By solving (33) and using (31), (32), one has

$$\rho^{(j+1)}(x) = \rho_0 + \sum_{i=0}^{j} r^{(i)}(x), \quad j \geq 0, \tag{36}$$

and the iterations are stopped when the condition

$$e \equiv \frac{1}{N}\left(\sum_{n=1}^{N}\left(\frac{\lambda_n^{C(exp)} - \lambda_n^{C}(\rho^{(j)})}{\lambda_n^{C(exp)}}\right)^2\right)^{\frac{1}{2}} + \frac{1}{M}\left(\sum_{m=1}^{M}\left(\frac{\lambda_m^{F(exp)} - \lambda_m^{F}(\rho^{(j)})}{\lambda_m^{F(exp)}}\right)^2\right)^{\frac{1}{2}} < \gamma \tag{37}$$

is satisfied for a small given number γ.

The convergence of the iterative procedure described above can be studied by extending the methods shown in [73], where finite eigenvalue data coming from a single spectrum only were used. Referring the interested reader to the paper [73] for the mathematical details of the convergence proof, here we recall the main result for the present reconstruction method in case of smooth mass variations. There exists a positive number $\widehat{\epsilon}_\rho$, $\widehat{\epsilon}_\rho$ only depending on the a priori data of the inverse problem, such that if $\epsilon \leq \widehat{\epsilon}_\rho$, then the iterative procedure of identification converges uniformly to a continuous function in $[0, L]$, provided that $|\boldsymbol{\delta\lambda}^{(0)}| < 1$, where $|\boldsymbol{\delta\lambda}^{(0)}|$ is the Euclidean norm of the vector $\boldsymbol{\delta\lambda}^{(0)}$. The convergence result clearly has local character, since its proof holds on the assumption that the mass variation is a small perturbation of the total mass of the unperturbed nanorod. It should be noticed, in addition, that the local character is also reflected on the condition $|\boldsymbol{\delta\lambda}^{(0)}| < 1$, which requires that the first N, M eigenvalues of the unperturbed nanorod under clamped and clamped-free end conditions, respectively, must be close enough to the corresponding target eigenvalues.

4. Applications

4.1. Numerical setting and test specimen

In order to evaluate the performance of the reconstruction method, we have used an extended version of the numerical code originally developed in [73]. The code is based on a finite element model of the nanobeam, with third-degree polynomial spline approximation of the axial displacement in each finite element.

The spatial mesh consists of N_e equally spaced finite elements, and the mass coefficient is approximated by a continuous, piecewise linear function on each finite element. Most of the simulations have been performed taking $N_e = 200$ and using the same number of frequencies from both spectra, e.g., $M = N$, with N up to 15. Local mass and stiffness matrices were evaluated in exact form, and the entries of the matrix $\mathbf{A}$ were determined by a trapezoidal rule of integration. The entire procedure, both for the direct and the inverse problem, was built in Scilab environment (version 5.5.2). The computation time needed for a single iteration of the identification algorithm (for $N_e = 200$ and with $N = M = 15$) was about 1 second. We refer to [73] (Section 5.2) for more details on the numerical procedure.

Concerning the test specimen, reference is made to the geometrical and material properties of the nanorod used in [49] and [73]. The radius R of the circular equivalent cross-section is equal to 50 μm and the length L is taken equal to 40 R; the material length scale parameters are assumed to be equal, and $\ell_0 = \ell_1 = 17.6$ μm; the Young's modulus E is equal to 1.44 GPa; the Poisson's coefficient is $\nu = 0.38$; and the volume mass density is equal to $\rho_{vol} = 1000$ kg/m^3. The coefficients a, b, ρ_0 corresponding to the above parameters take the value $a = 11.310$ N, $b = 3.554 \cdot 10^{-9}$ Nm^2, $\rho_0 = \rho_{vol} \cdot \pi R^2 = 7.854 \cdot 10^{-6}$ kg/m.

The method has been tested on an extended series of simulations, by varying, among other parameters, the number M, N of the first eigenfrequencies and the geometry of the mass variation (e.g., position, intensity, regularity). In particular, two main classes of mass variations will be considered hereinafter, namely, smooth or discontinuous mass functions $r_\epsilon(x)$, see Figure 1. The results of identification for free-error data are presented first, that is, only errors due to numerical approximation are included in the following analysis.

Before presenting the results, we recall that a preliminary series of tests were carried out in order to select a suitable mesh size for the numerical solution of the direct and inverse eigenvalue problem. The analysis suggests to assume a

mesh with $N_e = 200$ equally spaced finite elements, which turns out to be a good compromise between accuracy (maximum error on the first $N = M = 15$ eigenvalues less than $6.4 \cdot 10^{-5}$ percent) and computational cost for all the cases studied, including the reconstruction procedure. Moreover, preliminary tests suggest to choose $\gamma = 10^{-5}$ in the stopping criterion (37).

4.2. Identification of smooth mass coefficients

The identification of smooth coefficients (e.g., continuous mass distribution) leads to good results. Figures 2-4 show typical reconstructions of the mass density

$$\rho(x) = \rho_0 + \rho_0 t \cos^2\left(\frac{\pi(x-s)}{c}\right) \chi_{[s-\frac{c}{2}, s+\frac{c}{2}]}, \tag{38}$$

where $\chi_{[L_1,L_2]}$ is the characteristic function of the interval $[L_1, L_2]$, s is the central point of the support of the mass variation, c is the length of the support, $\rho_0 t$ is the maximum amplitude of variation, see Figure 1(a). For the sake of completeness, let us recall that the characteristic function $\chi_I : \mathbb{R} \to \mathbb{R}$ of the closed interval I, $I \subset \mathbb{R}$, is defined as $\chi_I(x) = 1$ if $x \in I$, $\chi_I(x) = 0$ if $x \in \mathbb{R} \setminus I$. The results for the two challenging cases corresponding to small mass increase and large mass increase, both supported in a small interval, (e.g., $s/L = 0.35$, $c/L = 0.1$, $t = 0.1$ and $s/L = 0.35$, $c/L = 0.1$, $t = 1$, respectively) are presented for $N = M$ in Figure 2 and 3. The global mass change ranges from 0.5% to 5.0% of the initial mass $\rho_0 L$, for ($\frac{c}{L} = 0.10,\ t = 0.10$) and ($\frac{c}{L} = 0.10,\ t = 1.0$), respectively.

We see that, in the first case, the identified coefficient agrees well with the exact one, and accuracy of reconstruction rapidly improves as N increases. Similar properties hold for the second case, apart from the oscillatory character of the reconstructed coefficient around the actual mass value, which is more evident for $N = 9$, whereas it becomes almost negligible when $N = 15$. Few iterations are sufficient to satisfy the convergence criterion (37) with $\gamma = 10^{-5}$, e.g., less than five in the present cases. For the sake of completeness, it should be noted

that part of our results involve not necessarily small mass variations, see, for example, Figure 4, with mass change equal to 15 per cent of the initial mass $\rho_0 L$. This would suggest that the proposed reconstruction method has some unexpected potential, in spite of the fact that the convergence of the identification procedure has local character and requires to work in a sufficiently small neighborhood of the referential nanorod.

In Table 1 some synthetic information concerning the sequence of iterations is reported. At most four iterations are required to fulfill the convergence criterion in all the cases considered. The quantity e defined as the average difference between identified and target eigenvalues, see equation (37), is reduced at each step of $1-2$ orders of magnitude. The L^2 and L^∞ errors on the mass coefficient estimate are both reduced through the iterations. In particular, for $M = N = 15$ the relative errors in L^2 and L^∞ norm are less than 7% and 5% of the initial values, respectively, confirming the accuracy in reconstructing smooth mass distributions. It should be also pointed out that the matrix $\mathbf{A}^{(j)}$ is always well conditioned during the iterations, with condition number $\kappa(\mathbf{A}^{(j)}) = \|\mathbf{A}^{(j)}\| \, \|(\mathbf{A}^{(j)})^{-1}\|$ ranging between 30 and 200 in all the cases studied. Here, $\|\mathbf{A}^{(j)}\| = \max_{|\mathbf{y}|=1} |\mathbf{A}^{(j)}\mathbf{y}|$, where $|\mathbf{y}| = \sqrt{\mathbf{y}\cdot\mathbf{y}}$ is the Euclidean norm of the vector $\mathbf{y} \in \mathbb{R}^{N+M}$.

We briefly discuss the results of the reconstruction when a different number of resonant frequencies belonging to the two spectra is chosen. The closed-form solution of the inverse linearized problem in the neighborhood of the uniform nanorod presented above shows that, in the extreme case in which the frequency data belong to the single spectrum under clamped end conditions, only the even generalized Fourier coefficients of the first-order mass variation can be determined. As a consequence, the reconstructed mass variation is symmetric with respect to the mid-point $x = L/2$ and shows an appreciable increase of the mass density exactly inside the actual region of the interval $[0, L/2]$ affected by the mass change, see, for instance, Figure 5. The estimate of the mass

density amplitude, however, is rather inaccurate, showing an underestimate of about 50%. This indeterminacy is typical of the identification in symmetrical systems by eigenvalue data only, and it has been found also in other contexts, see, for example, the identification of damage in full-scale beams performed in [79] (see Figure 9 of this reference). When, on the other hand, only the resonant frequencies of the clamped-free spectrum are used, our numerical simulations show that the graph of the mass variation is approximately odd with respect to $x = L/2$. Therefore, in case of positive mass variations (i.e., $r_\epsilon(x) \geq 0$), this implies a significant difference between identified and exact coefficient, as it is shown in Figure 6. Finally, significant discrepancy was also found in the intermediate cases in which $N \neq M$, primarily since some generalized Fourier coefficients are missing in the expression of $r_\epsilon(x)$, see Figure 7. Basing on the above considerations and results, our experience suggests that it is preferable to use the same number of first frequencies in both spectra. It can be shown that similar conclusions can be drawn in determining discontinuous mass variations.

4.3. Identification of discontinuous mass coefficients

The determination of discontinuous mass coefficients is more problematic, since it is expected that the reconstruction may fail near the jump discontinuities. Some representative results are shown for the coefficient

$$\rho(x) = \rho_0 + \rho_0 t \cdot \chi_{[s-\frac{c}{2}, s+\frac{c}{2}]}, \tag{39}$$

where s, c, t have the same meaning as in the previous section, see Figure 1(b). These cases correspond to perturbation located near the left end of the nanorod ($s/L = 0.15$) and with small support ($c/L = 0.1$), but having either small ($t = 0.1$, case i)) or large ($t = 1.0$, case ii)) intensity, respectively. In case i) (see Figure 8), the results are accurate enough for $N = 12 - 15$, whereas oscillations of the identified mass coefficient have appreciable amplitude in case ii) (see Figure 9), and propagate in the remaining part of the interval. As it

was expected, pointwise estimates of the mass change fail near the jumps. The support of the mass perturbation is slightly overestimated, whereas it turns out that the mean value of the mass change is estimated with good accuracy.

Numerical results also show that the reconstruction of large mass variations is accurate enough, see Figure 10, although a large number of frequencies (e.g., $M = N = 20 - 25$ with $N_e = 400$) and more iterations (less than 10) are needed to reduce the oscillatory character of the identified mass profile, see Figure 11. Regarding this point, we recall that when the present method is combined with the physical a priori information that the mass variation is positive, the reconstruction of discontinuous distributions may further be improved, leading to better uniform approximation of the actual solution. We refer to [73] (Section 5.3.4) for more details and applications.

4.4. Application to noisy data

In order to test the robustness of the method, the identification was carried out by perturbing the target noise-free resonant frequencies belonging to the two spectra $\sqrt{\lambda_n^{exp}}$ as follows

$$\sqrt{\lambda_n^{exp-err}} = \sqrt{\lambda_n^{exp}} + \tau_n. \tag{40}$$

Here, τ_n is a random Gaussian variable with vanishing mean and standard deviation σ such that $3\sigma = 2\pi\Pi$, where Π is the maximum admitted error in the frequency measurements. The effect of errors was evaluated both for smooth and discontinuous mass distributions, by considering different profile of the coefficient and by varying the number $N = M$ of the first eigenfrequencies used in identification, for increasing values of Π ranging from 100 Hz to 5000 Hz. A selected, though representative, set of results is shown in Figures 12 and 13, for smooth and discontinuous mass coefficients, respectively. For each position along the nanorod axis, and besides the exact mass coefficient, every subfigure contains three curves: the curve of the mean value and the two curves obtained

by adding $\pm 3\sigma$ to the mean value. One thousand of simulations was performed for each case. It turns out that the three curves are almost indistinguishable for $\Pi = 100$ Hz. Appreciable discrepancy occurs for $\Pi = 1000$ Hz, and for Π greater than 3000 Hz the quality of the reconstruction is poor. In particular, for Π less than 2000 Hz, the effect of errors makes it possible to discriminate the presence of even minor variations of mass, either regular or discontinuous, and for which the influence of errors on the data is expected to be more significant. It should be noted that $\Pi = 2000$ Hz corresponds to percentage errors ranging approximately from 0.05 (high frequency) to 0.65 (low frequency) per cent of the unperturbed first fifteen resonant frequencies. Finally, the convergence speed of the iterative method is not significantly affected by the random noise, and the number of iterations needed to get convergence is slightly bigger than in the error-free case.

5. Conclusions

In this paper we have studied the problem of identifying a general distributed mass added to a nanorod by using the variations produced on a suitable set of lower resonant frequencies of the longitudinal vibration. In the previous work [73], it was shown that the mass coefficient can be determined under the hypothesis that the added mass is small with respect to the total mass of the nanosensor, and the first N frequencies under clamped boundary conditions are known. The result obtained in [73] holds only when it is a priori known that the support of the mass variation belongs to a half of the nanorod interval. In this paper, this a priori assumption has been removed and a constructive procedure for determining general mass coefficients has been proposed. More precisely, the a priori information on the support location of the mass variation is replaced by the knowledge of the first M resonant frequencies of the nanorod under clamped-free boundary conditions. Under these assumptions, and always retaining the assumption of small mass variation, we construct an approximation

of the unknown mass distribution by means of a generalized Fourier sum of order $(N + M)$, whose coefficients are calculated in terms of the variations of the eigenvalues belonging to the two partial spectra.

The mathematical aspects related to the convergence of the iterative identification method have been comprehensively treated in [73], and have not been repeated here. Rather, we focused on applications. The results obtained in an extended series of numerical simulations show that good accuracy is reached for $N = M$. In particular, if the mass coefficient is regular, then even a suitable number of frequencies, say N less than 10, is sufficient to obtain an accurate uniform approximation. In case of rough coefficients (e.g., discontinuous), a larger number of information is necessary to capture the real behavior, say $N = 15 - 20$.

Most frequently, inertial imaging methods used with nanomechanical systems use classical elasticity theories to model the dynamic behavior of the sensor. However, the identification method herein presented is capable of accounting for size effects experimentally observed at the micron scale. This makes this technique particularly suitable for nanosensors using axial vibration behavior for ultrasensitive detection of analytes in chemical or biological applications.

Finally, it is interesting to note that, despite the great mathematical difficulties typical of this class of inverse eigenvalue problems with finite data, the results of numerical simulations are unexpectedly good, even for added masses that are not necessarily small and also in the presence of errors in the data. These results encourage to deepen the study of this class of inverse problems from at least two points of view. On the one hand, it would be important to quantify the convergence rate of the iterative procedure, and study the convergence as the number of frequencies considered as input data increases. On the other hand, the theory we have developed is probably mature to include the much more complex and challenging problem of the determination of mass variations in nanobeams from finite number of resonant frequencies of the bending

vibration. Both the issues are currently under study by the authors, and some preliminary results are rather promising.

Acknowledgements

The authors from Universidad Carlos III de Madrid wish to acknowledge *Ministerio de Economía y Competitividad de España* for the financial support, under Grant number DPI2014-57989-P. The authors from University of Udine gratefully acknowledge the financial support of the National Research Project PRIN 2015TT JN95 'Identification and monitoring of complex structural systems'.

References

[1] X. Li, H. Yu, X. Gan, X. Xia, P. Xu, J. Li, M. Liu, Y. Li, Integrated MEMS/NEMS resonant cantilevers for ultrasensitive biological detection, Journal of Sensors 2009, DOI:10.1155/2009/637874.

[2] B. Arash, Q. Wang, Detection of gas atoms with carbon nanotubes, Scientific Reports 3 (2013) Article number 1782.

[3] G. Rius, F. Pérez-Múrano, Nanocantilever Beams: Modeling, Fabrication, and Applications, CRC Press, 2015, Ch. Nanocantilever beam fabrication for CMOS technology integration.

[4] A. Morassi, M. Dilena, On point mass identification in rods and beams from minimal frequency mesurements, Inverse Problems in Engineering 10 (2002) 183–201.

[5] L. Rubio, J. Fernández-Sáez, A. Morassi, Point mass identification in rectangular plates from minimal natural frequency data, Mechanical Systems and Signal Processing 80 (2016) 245–261.

[6] L. Rubio, J. Fernández-Sáez, A. Morassi, Crack identification in non-uniform rods by two frequency data, International Journal of Solids and Structures 75-76 (2015) 61–80.

[7] L. Rubio, J. Fernández-Sáez, A. Morassi, Identification of an open crack in a beam with variable profile by two resonant frequencies, Journal of Vibration and Control 24 (15) (2018) 839–859.

[8] S. Cuenot, S. Demoustier-Champagne, B. Nysten, Elastic modulus of polypyrrole nanotubes, Physical Review Letters 85 (8) (2000) 1690–1693.

[9] D. C. C. Lam, F. Yang, A. C. M. Chong, J. Wang, P. Tong, Experiments and theory in strain gradient elasticity, Journal of the Mechanics and Physics of Solids 51 (2003) 1477–1508.

[10] S. Cuenot, C. Frétigny, S. Demoustier-Champagne, B. Nysten, Surface tension effect on the mechanical properties of nanomaterials measured by atomic force microscopy, Physical Review B 69 (16) (2004) Article number 165410.

[11] C. Chen, Y. Shi, Y. S. Zhang, J. Zhu, Y. Yan, Size dependence of Young's modulus in ZnO nanowires, Physical Review Letters 96 (7) (2006) Article number 075505.

[12] A. C. Eringen, Microcontinuum field theories: I. Foundations and solids, Springer Science & Business Media, 2012.

[13] E. Cosserat, F. Cosserat, Theory of Deformable Bodies, (Translated by D.H. Delphenich), Scientific Library, A. Hermann and Sons, Paris, 1909.

[14] M. Shaat, A reduced micromorphic model for multiscale materials and its applications in wave propagation, Composite Structures 201 (2018) 446–454.

[15] R. Ansari, A. Norouzzadeh, A. Shakouri, M. Bazdid-Vahdati, H. Rouhi, Finite element analysis of vibrating micro-beams and-plates using a three-dimensional micropolar element, Thin-Walled Structures 124 (2018) 489–500.

[16] E. Kröner, Elasticity theory of materials with long range cohesive forces, International Journal of Solids and Structures 3 (1967) 731–742.

[17] J. Krumhansl, Some considerations of the relation between solid state physics and generalized continuum mechanics, in: E. Kröner (Ed.), Mechanics of Generalized Continua. IUTAM Symposia. Springer, Berlin Heidelberg, 1968, pp. 298–311.

[18] I. A. Kunin, The theory of elastic media with microstructure and the theory of dislocations, in: E. Kröner (Ed.), Mechanics of Generalized Continua. IUTAM Symposia. Springer, Berlin Heidelberg, 1968, pp. 321–329.

[19] A. C. Eringen, Linear theory of nonlocal elasticity and dispersion of plane-waves, International Journal of Engineering Science 10 (5) (1972) 233–248.

[20] A. C. Eringen, Nonlocal polar elastic continua, International Journal of Engineering Science 10 (1) (1972) 1–16.

[21] A. C. Eringen, D. G. B. Edelen, Nonlocal elasticity, International Journal of Engineering Science 10 (3) (1972) 233–248.

[22] A. C. Eringen, On differential-equations of nonlocal elasticity and solutions of screw dislocation and surface-waves, Journal of Applied Physics 54 (9) (1983) 4703–4710.

[23] M. A. Eltaher, M. E. Khater, S. A. Emam, A review on nonlocal elastic models for bending, buckling, vibrations, and wave propagation of nanoscale beams, Applied Mathematical Modelling 40 (2016) 4109–4128.

[24] H. Rafii-Tabar, E. Ghavanloo, S. A. Fazelzadeh, Nonlocal continuum-based modeling of mechanical characteristics of nanoscopic structures, Physics Reports 638 (2016) 1–97.

[25] H. T. Thai, T. P. Vo, T. K. Nguyen, S. E. Kim, A review of continuum mechanics models for size-dependent analysis of beams and plates, Composite Structures 177 (2017) 196–219.

[26] J. Peddieson, G. R. Buchanan, R. P. McNitt, Application of nonlocal continuum models to nanotechnology, International Journal of Engineering Science 41 (3-5) (2003) 305–312.

[27] G. Romano, R. Barretta, M. Diaco, F. Marotti de Sciarra, Constitutive boundary conditions and paradoxes in nonlocal elastic nanobeams, International Journal of Mechanical Sciences 121 (2017) 151–156.

[28] G. Romano, R. Barretta, Stress-driven versus strain-driven nonlocal integral model for elastic nano-beams, Composites Part B 114 (2017) 184–188.

[29] A. Apuzzo, R. Barretta, R. Luciano, F. M. de Sciarra, R. Penna, Free vibrations of Bernoulli-Euler nano-beams by the stress-driven nonlocal integral model, Composites Part B: Engineering 123 (2017) 105–111.

[30] R. Barretta, M. Canadija, R. Luciano, F. M. de Sciarra, Stress-driven modeling of nonlocal thermoelastic behavior of nanobeams, International Journal of Engineering Science 126 (2018) 53–67.

[31] R. Barretta, S. A. Faghidian, R. Luciano, Longitudinal vibrations of nanorods by stress-driven integral elasticity, Mechanics of Advanced Materials and Structures (2018) 1–9.

[32] R. Barretta, R. Luciano, F. M. de Sciarra, G. Ruta, Stress-driven nonlocal integral model for Timoshenko elastic nano-beams, European Journal of Mechanics-A/Solids 72 (2018) 275–286.

[33] E. Mahmoudpour, S. Hosseini-Hashemi, S. Faghidian, Nonlinear vibration analysis of FG nano-beams resting on elastic foundation in thermal environment using stress-driven nonlocal integral model, Applied Mathematical Modelling 57 (2018) 302–315.

[34] A. C. Eringen, Theory of nonlocal elasticity and some applications, Res Mechanica 21 (4) (1987) 313–342.

[35] P. Khodabakhshia, J. N. Reddy, A unified integro-differential nonlocal model, International Journal of Engineering Science 95 (2015) 60–75.

[36] Y. B. Wang, X. W. Zhu, H. H. Dai, Exact solutions for the static bending of Euler-Bernoulli beams using Eringen's two-phase local/nonlocal model, AIP Advances 6 (8) (2016) Article number 085114.

[37] X. Zhu, Y. Wang, H. H. Dai, Buckling analysis of Euler-Bernoulli beams using Eringen's two-phase nonlocal model, International Journal of Engineering Science 1116 (2017) 130–140.

[38] K. Eptaimeros, C. C. Koutsoumaris, G. Tsamasphyros, Nonlocal integral approach to the dynamical response of nanobeams, International Journal of Mechanical Science 115–116 (2016) 68–80.

[39] J. Fernández-Sáez, R. Zaera, Vibrations of Bernoulli-Euler beams using the two-phase nonlocal elasticity theory, International Journal of Engineering Science 119 (2017) 232–248.

[40] R. Barretta, F. Fabbrocino, R. Luciano, F. M. de Sciarra, Closed-form solutions in stress-driven two-phase integral elasticity for bending of functionally graded nano-beams, Physica E: Low-dimensional Systems and Nanostructures 97 (2018) 13–30.

[41] R. Barretta, S. A. Faghidian, R. Luciano, C. Medaglia, R. Penna, Stress-

driven two-phase integral elasticity for torsion of nano-beams, Composites Part B: Engineering 145 (2018) 62–69.

[42] R. A. Toupin, Elastic materials with couple-stresses, Archive for Rational Mechanics and Analysis 11 (5) (1962) 385–414.

[43] R. D. Mindlin, H. F. Tiersten, Effects of couple-stresses in linear elasticity, Archive for Rational Mechanics and Analysis 11 (5) (1962) 415–448.

[44] R. A. Toupin, Theories of elasticity with couple-stress, Archive for Rational Mechanics and Analysis 17 (2) (1964) 85–112.

[45] R. D. Mindlin, Micro-structure in linear elasticity, Archive for Rational Mechanics and Analysis 16 (1964) 51–78.

[46] R. D. Mindlin, Second gradient of strain and surface-tension in linear elasticity, International Journal of Solids and Structures 1 (1965) 417–438.

[47] F. Yang, A. Chong, D. Lam, P. Tong, Couple stress based strain gradient theory for elasticity, International Journal of Solids and Structures 39 (2002) 2731–2743.

[48] N. A. Fleck, J. W. Hutchinson, Strain gradient plasticity, Advances in Applied Mechanics 33 (1997) 295–361.

[49] S. Kong, S. Zhou, Z. Nie, K. Wang, Static and dynamic analysis of micro-beams based on strain gradient elasticity theory, International Journal of Engineering Science 47 (2009) 487–498.

[50] B. Wang, J. Zhao, S. Zhou, A microscale Timoshenko beam model based on strain gradient elasticity theory, European Journal of Mechanics A-Solids 29 (2010) 837–843.

[51] B. Akgoz, O. Civalek, Strain gradient elasticity and modified couple stress models for buckling analysis of axially loaded micro-scaled beams, International Journal of Engineering Science 49 (2011) 1268–1280.

[52] B. Akgoz, O. Civalek, A new trigonometric beam model for buckling of strain gradient microbeams, International Journal of Mechanical Sciences 81 (2014) 88–94.

[53] M. H. Kahrobaiyan, M. Asghari, M. T. Ahmadian, Strain gradient beam element, Finite Elements in Analysis and Design 68 (2013) 63–75.

[54] B. Zhang, Y. He, D. Liu, Z. Gan, L. Shen, Non-classical Timoshenko beam element based on the strain gradient elasticity theory, Finite Elements in Analysis and Design 79 (2014) 22–39.

[55] C. Lim, G. Zhang, J. Reddy, A higher-order nonlocal elasticity and strain gradient theory and its applications in wave propagation, Journal of the Mechanics and Physics of Solids 78 (2015) 298–313.

[56] L. Li, X. Li, Y. Hu, Free vibration analysis of nonlocal strain gradient beams made of functionally graded material, International Journal of Engineering Science 102 (2016) 77–92.

[57] M. Şimşek, Nonlinear free vibration of a functionally graded nanobeam using nonlocal strain gradient theory and a novel Hamiltonian approach, International Journal of Engineering Science 105 (2016) 12–27.

[58] X. Zhu, L. Li, Closed form solution for a nonlocal strain gradient rod in tension, International Journal of Engineering Science 119 (2017) 16–28.

[59] X.-J. Xu, X.-C. Wang, M.-L. Zheng, Z. Ma, Bending and buckling of nonlocal strain gradient elastic beams, Composite Structures 160 (2017) 366–377.

[60] L. Lu, X. Guo, J. Zhao, A unified nonlocal strain gradient model for nanobeams and the importance of higher order terms, International Journal of Engineering Science 119 (2017) 265–277.

[61] R. Barretta, F. M. de Sciarra, Constitutive boundary conditions for nonlocal strain gradient elastic nano-beams, International Journal of Engineering Science 130 (2018) 187–198.

[62] A. Apuzzo, R. Barretta, S. Faghidian, R. Luciano, F. M. de Sciarra, Free vibrations of elastic beams by modified nonlocal strain gradient theory, International Journal of Engineering Science 133 (2018) 99–108.

[63] M. Simsek, Some closed-form solutions for static, buckling, free and forced vibration of functionally graded (FG) nanobeams using nonlocal strain gradient theory, Composite Structures (2019) doi: https://doi.org/10.1016/j.compstruct.2019.111041.

[64] R. Zaera, Ó. Serrano, J. Fernández-Sáez, On the consistency of the nonlocal strain gradient elasticity, International Journal of Engineering Science 138 (2019) 65–81.

[65] M. E. Gurtin, A. I. Murdoch, A continuum theory of elastic material surfaces, Archive for Rational Mechanics and Analysis 57 (4) (1975) 291–323.

[66] M. E. Gurtin, A. I. Murdoch, Surface stress in solids, International Journal of Solids and Structures 14 (6) (1978) 431–440.

[67] S. A. Mirkalantari, M. Hashemian, S. A. Eftekhari, D. Toghraie, Pull-in instability analysis of rectangular nanoplate based on strain gradient theory considering surface stress effects, Physica B: Condensed Matter 519 (2017) 1–14.

[68] G. Fu, S. Zhou, L. Qi, A size-dependent Bernoulli–Euler beam model based on strain gradient elasticity theory incorporating surface effects, ZAMM-

Journal of Applied Mathematics and Mechanics/Zeitschrift für Angewandte Mathematik und Mechanik (2019) e201800048.

[69] A. Morassi, J. Fernández-Sáez, R. Zaera, J. A. Loya, Resonator-based detection in nanorods, Mechanical Systems and Signal Processing 93 (2017) 645–660.

[70] M. Dilena, M. Fedele Dell'Oste, J. Fernández-Sáez, A. Morassi, R. Zaera, Mass detection in nanobeams from bending resonant frequency shifts, Mechanical Systems and Signal Processing 116 (2019) 261–276.

[71] J. Fernández-Sáez, A. Morassi, L. Rubio, R. Zaera, Transverse free vibration of resonant nanoplate mass sensors: identification of an attached point mass, International Journal of Mechanical Sciences 150 (2019) 217–225.

[72] M. S. Hanay, S. I. Kelber, C. D. O'Connell, P. Mulvaney, J. E. Sader, M. L. Roukes, Inertial imaging with nanomechanical systems, Nature Nanotechnology 10 (4) (2015) 339–344.

[73] M. Dilena, M. Fedele Dell'Oste, J. Fernández-Sáez, A. Morassi, R. Zaera, Recovering added mass in nanoresonator sensors from finite axial eigenfrequency data, Mechanical Systems and Signal Processing 130 (2019) 122–151.

[74] D. C. Barnes, The inverse eigenvalue problem with finite data, SIAM Journal on Mathematical Analysis 22 (3) (1991) 732–753.

[75] V. Barcilon, On the uniqueness of inverse eigenvalue problems, Geophysical Journal of the Royal Astronautic Society 39 (1974) 287–298.

[76] G. Gladwell, Inverse Problems in Vibration, 2nd edn, Kluwer, Dordrecht, The Netherlands, 2004.

[77] A. Schueller, Uniqueness for near-constant data in fourth-order inverse eigenvalue problems, Journal of Mathematical Analysis and Applications 258 (2001) 658–670.

[78] B. Akgoz, O. Civalek, Longitudinal vibration analysis for microbars based on strain gradient elasticity theory, Journal of Vibration and Control 20 (2014) 606–616.

[79] A. Bilotta, A. Morassi, E. Turco, The use of quasi-isospectral operators for damage detection in rods, Meccanica 53 (2018) 319–345.

Table Captions

Table 1. Some results of the reconstruction of smooth mass changes as in (38) versus iteration number j (up to convergence), with (a): $\frac{s}{L} = 0.35$, $\frac{c}{L} = 0.10$, $t = 0.10$ (Figure 2); (b): $\frac{s}{L} = 0.35$, $\frac{c}{L} = 0.10$, $t = 1.00$ (Figure 3); (c): $\frac{s}{L} = 0.35$, $\frac{c}{L} = 0.30$, $t = 1.00$ (Figure 4), using the first $N = 6$ (columns $2-5$), $N = 15$ (columns $6-9$) eigenfrequencies. The quantity e is defined in (37); $e_{L^2} = \frac{\|\rho^{ident} - \rho^{exact}\|_{L^2}}{\|\rho^{exact}\|_{L^2}}$, $e_{L^\infty} = \frac{\|\rho^{ident} - \rho^{exact}\|_{L^\infty}}{\|\rho^{exact}\|_{L^\infty}}$, where $\rho^{ident} = \rho^{ident}(x)$, $\rho^{exact} = \rho^{exact}(x)$ are the identified and the exact mass density per unit length, respectively. $\kappa(\mathbf{A}^{(j)})$ is the condition number of the matrix $\mathbf{A}^{(j)}$. The unperturbed nanorod corresponds to $j = 0$.

Figure Captions

Figure 1. Mass density per unit length $\rho = \rho(x)$ to be identified in $[0, L]$. (a) Smooth mass changes as in (38); (b) discontinuous mass changes as in (39).

Figure 2. Reconstruction of smooth mass changes as in (38), with $\frac{s}{L} = 0.35$, $\frac{c}{L} = 0.10$, $t = 0.10$, using the first $N = M = 6, 9, 12, 15$ eigenfrequencies of both spectra.

Figure 3. Reconstruction of smooth mass changes as in (38), with $\frac{s}{L} = 0.35$, $\frac{c}{L} = 0.10$, $t = 1.00$, using the first $N = M = 6, 9, 12, 15$ eigenfrequencies of both spectra.

Figure 4. Reconstruction of smooth mass changes as in (38), with $\frac{s}{L} = 0.35$, $\frac{c}{L} = 0.30$, $t = 1.00$, using the first $N = M = 6, 9, 12, 15$ eigenfrequencies of both spectra.

Figure 5. Reconstruction of smooth mass changes as in (38), with $\frac{s}{L} = 0.35$, $\frac{c}{L} = 0.30$, $t = 1.00$, using only the first $N = 6, 9, 12, 15$ eigenfrequencies of the clamped nanorod.

Figure 6. Reconstruction of smooth mass changes as in (38), with $\frac{s}{L} = 0.35$, $\frac{c}{L} = 0.30$, $t = 1.00$, using only the first $M = 6, 9, 12, 15$ eigenfrequencies of the clamped-free nanorod.

Figure 7. Reconstruction of smooth mass changes as in (38), with $\frac{s}{L} = 0.35$, $\frac{c}{L} = 0.30$, $t = 1.00$, using the first $(M, N) = (3, 15)$, $(M, N) = (9, 15)$, $(M, N) = (15, 3)$, $(M, N) = (15, 9)$ eigenfrequencies of the two spectra.

Figure 8. Reconstruction of discontinuous mass changes as in (39), with $\frac{s}{L} = 0.15$, $\frac{c}{L} = 0.10$, $t = 0.10$, using only the first $N = M = 6, 9, 12, 15$ eigenfrequencies of both spectra.

Figure 9. Reconstruction of discontinuous mass changes as in (39), with $\frac{s}{L} = 0.15$, $\frac{c}{L} = 0.10$, $t = 1.00$, using the first $N = M = 6, 9, 12, 15$ eigenfrequencies of both spectra.

Figure 10. Reconstruction of discontinuous mass changes as in (39), with $\frac{s}{L} = 0.35$, $\frac{c}{L} = 0.30$, $t = 1.00$, using the first $N = M = 6, 9, 12, 15$ eigenfrequencies of both spectra.

Figure 11. Reconstruction of discontinuous mass changes as in (39), with $\frac{s}{L} = 0.35$, $\frac{c}{L} = 0.30$, $t = 1.00$, using the first $N = M = 20, 25$ eigenfrequencies.

Figure 12. Noise effects on identification of smooth mass changes. Upper row: mass changes as in (38), with $\frac{s}{L} = 0.35$, $\frac{c}{L} = 0.10$, $t = 0.10$. Lower row: mass changes as in (38), with $\frac{s}{L} = 0.35$, $\frac{c}{L} = 0.30$, $t = 1.00$.

Figure 13. Noise effects on identification of discontinuous mass changes. Upper row: mass changes as in (39), with $\frac{s}{L} = 0.15$, $\frac{c}{L} = 0.10$, $t = 0.10$. Lower row: mass changes as in (39), with $\frac{s}{L} = 0.35$, $\frac{c}{L} = 0.30$, $t = 1.00$.

Table 1: Some results of the reconstruction of smooth mass changes as in (38) versus iteration number j (up to convergence), with (a): $\frac{s}{L} = 0.35$, $\frac{c}{L} = 0.10$, $t = 0.10$ (Figure 2); (b): $\frac{s}{L} = 0.35$, $\frac{c}{L} = 0.10$, $t = 1.00$ (Figure 3); (c): $\frac{s}{L} = 0.35$, $\frac{c}{L} = 0.30$, $t = 1.00$ (Figure 4), using the first $N = 6$ (columns 2 5), $N = 15$ (columns 6 9) eigenfrequencies. The quantity e is defined in (37); $e_{L^2} = \frac{\|\rho^{ident} - \rho^{exact}\|_{L^2}}{\|\rho^{exact}\|_{L^2}}$, $e_{L^\infty} = \frac{\|\rho^{ident} - \rho^{exact}\|_{L^\infty}}{\|\rho^{exact}\|_{L^\infty}}$, where $\rho^{ident} = \rho^{ident}(x)$, $\rho^{exact} = \rho^{exact}(x)$ are the identified and the exact mass density per unit length, respectively. $\kappa(\mathbf{A}^{(j)})$ is the condition number of the matrix $\mathbf{A}^{(j)}$. The unperturbed nanorod corresponds to $j = 0$.

(a)

j	e	$\kappa(\mathbf{A}^{(j)})$	e_{L^2}	e_{L^∞}	e	$\kappa(\mathbf{A}^{(j)})$	e_{L^2}	e_{L^∞}
0	$1.69 \cdot 10^{-3}$	$2.50 \cdot 10^{+1}$	$1.92 \cdot 10^{-2}$	$9.09 \cdot 10^{-2}$	$1.01 \cdot 10^{-3}$	$6.10 \cdot 10^{+1}$	$1.92 \cdot 10^{-2}$	$9.09 \cdot 10^{-2}$
1	$2.50 \cdot 10^{-5}$	$2.50 \cdot 10^{+1}$	$1.01 \cdot 10^{-2}$	$3.84 \cdot 10^{-2}$	$2.69 \cdot 10^{-5}$	$6.10 \cdot 10^{+1}$	$1.66 \cdot 10^{-3}$	$5.57 \cdot 10^{-3}$
2	$4.27 \cdot 10^{-8}$	$2.75 \cdot 10^{+1}$	$1.01 \cdot 10^{-2}$	$3.74 \cdot 10^{-2}$	$2.32 \cdot 10^{-7}$	$7.42 \cdot 10^{+1}$	$1.39 \cdot 10^{-3}$	$4.24 \cdot 10^{-3}$

(b)

j	e	$\kappa(\mathbf{A}^{(j)})$	e_{L^2}	e_{L^∞}	e	$\kappa(\mathbf{A}^{(j)})$	e_{L^2}	e_{L^∞}
0	$1.63 \cdot 10^{-2}$	$2.50 \cdot 10^{+1}$	$1.81 \cdot 10^{-1}$	$5.00 \cdot 10^{-1}$	$9.03 \cdot 10^{-3}$	$6.10 \cdot 10^{+1}$	$1.81 \cdot 10^{-1}$	$5.00 \cdot 10^{-1}$
1	$1.89 \cdot 10^{-3}$	$2.50 \cdot 10^{+1}$	$9.86 \cdot 10^{-2}$	$2.45 \cdot 10^{-1}$	$1.53 \cdot 10^{-3}$	$6.10 \cdot 10^{+1}$	$5.89 \cdot 10^{-2}$	$1.55 \cdot 10^{-1}$
2	$9.03 \cdot 10^{-5}$	$5.34 \cdot 10^{+1}$	$9.40 \cdot 10^{-2}$	$1.95 \cdot 10^{-1}$	$1.95 \cdot 10^{-4}$	$1.93 \cdot 10^{+2}$	$1.30 \cdot 10^{-2}$	$2.52 \cdot 10^{-2}$
3	$4.19 \cdot 10^{-7}$	$6.27 \cdot 10^{+1}$	$9.40 \cdot 10^{-2}$	$1.95 \cdot 10^{-1}$	$6.09 \cdot 10^{-6}$	$3.17 \cdot 10^{+2}$	$8.40 \cdot 10^{-3}$	$1.53 \cdot 10^{-2}$

(c)

j	e	$\kappa(\mathbf{A}^{(j)})$	e_{L^2}	e_{L^∞}	e	$\kappa(\mathbf{A}^{(j)})$	e_{L^2}	e_{L^∞}
0	$4.46 \cdot 10^{-2}$	$2.50 \cdot 10^{+1}$	$2.82 \cdot 10^{-1}$	$5.00 \cdot 10^{-1}$	$2.56 \cdot 10^{-2}$	$6.10 \cdot 10^{+1}$	$2.82 \cdot 10^{-1}$	$5.00 \cdot 10^{-1}$
1	$8.44 \cdot 10^{-3}$	$2.50 \cdot 10^{+1}$	$1.01 \cdot 10^{-1}$	$1.92 \cdot 10^{-1}$	$4.73 \cdot 10^{-3}$	$6.10 \cdot 10^{+1}$	$1.02 \cdot 10^{-1}$	$1.97 \cdot 10^{-1}$
2	$8.70 \cdot 10^{-4}$	$5.25 \cdot 10^{+1}$	$1.99 \cdot 10^{-2}$	$3.38 \cdot 10^{-2}$	$5.20 \cdot 10^{-4}$	$1.29 \cdot 10^{+2}$	$1.91 \cdot 10^{-2}$	$3.80 \cdot 10^{-2}$
3	$2.90 \cdot 10^{-5}$	$7.91 \cdot 10^{+1}$	$1.05 \cdot 10^{-2}$	$1.68 \cdot 10^{-2}$	$1.85 \cdot 10^{-5}$	$1.95 \cdot 10^{+2}$	$2.16 \cdot 10^{-3}$	$3.15 \cdot 10^{-3}$
4	$7.49 \cdot 10^{-8}$	$8.17 \cdot 10^{+1}$	$1.05 \cdot 10^{-2}$	$1.65 \cdot 10^{-2}$	$8.27 \cdot 10^{-8}$	$2.03 \cdot 10^{+2}$	$2.05 \cdot 10^{-3}$	$2.92 \cdot 10^{-3}$

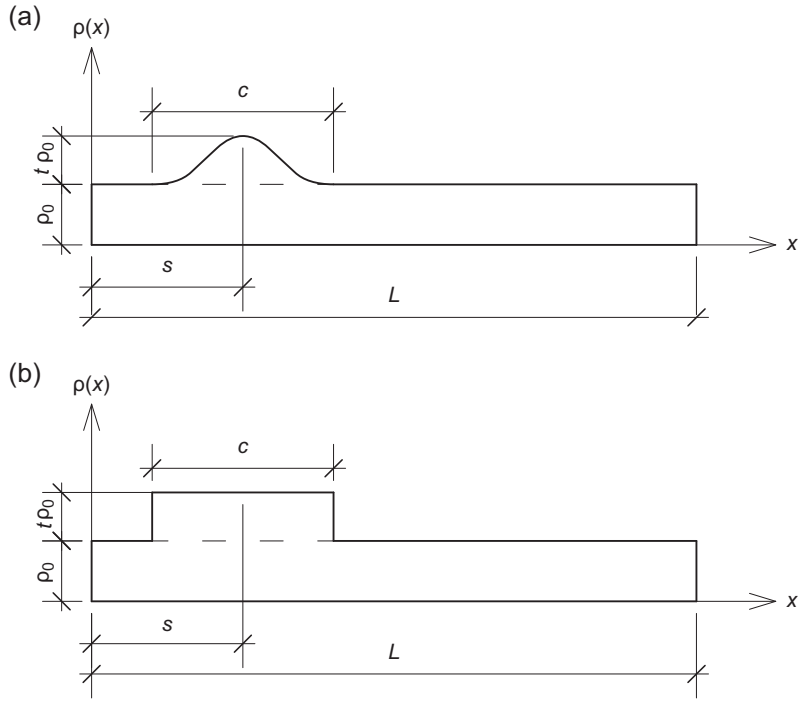

Figure 1: Mass density per unit length $\rho = \rho(x)$ to be identified in $[0, L]$. (a) Smooth mass changes as in (38); (b) discontinuous mass changes as in (39).

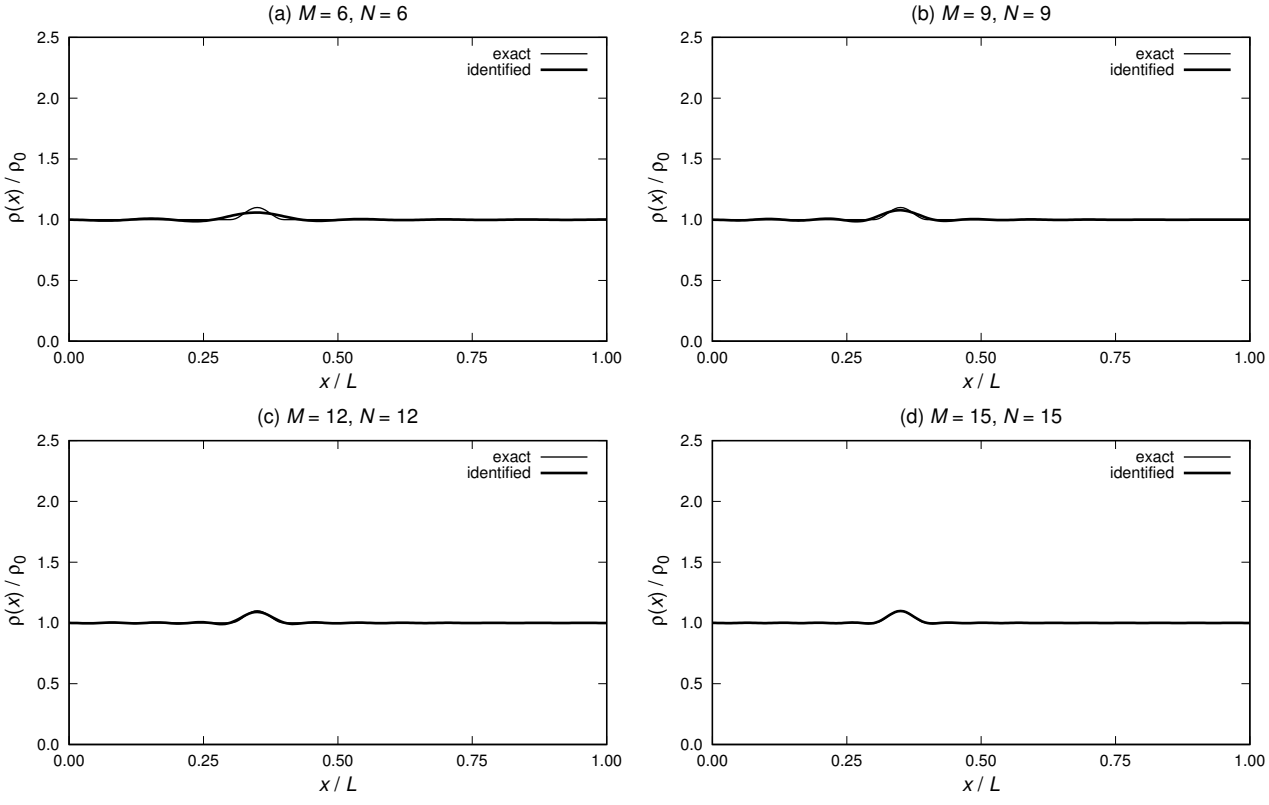

Figure 2: Reconstruction of smooth mass changes as in (38), with $\frac{s}{L} = 0.35$, $\frac{c}{L} = 0.10$, $t = 0.10$, using the first $N = M = 6, 9, 12, 15$ eigenfrequencies of both spectra.

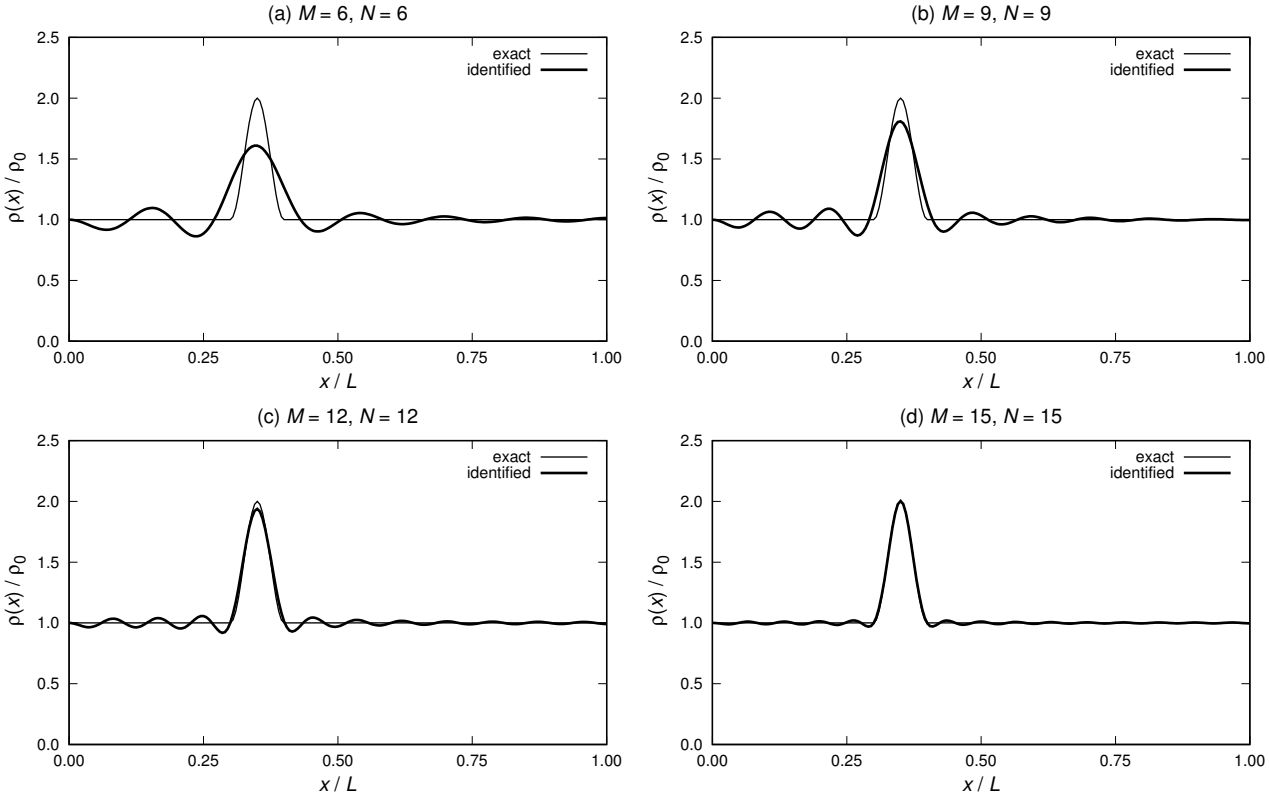

Figure 3: Reconstruction of smooth mass changes as in (38), with $\frac{s}{L} = 0.35$, $\frac{c}{L} = 0.10$, $t = 1.00$, using the first $N = M = 6, 9, 12, 15$ eigenfrequencies of both spectra.

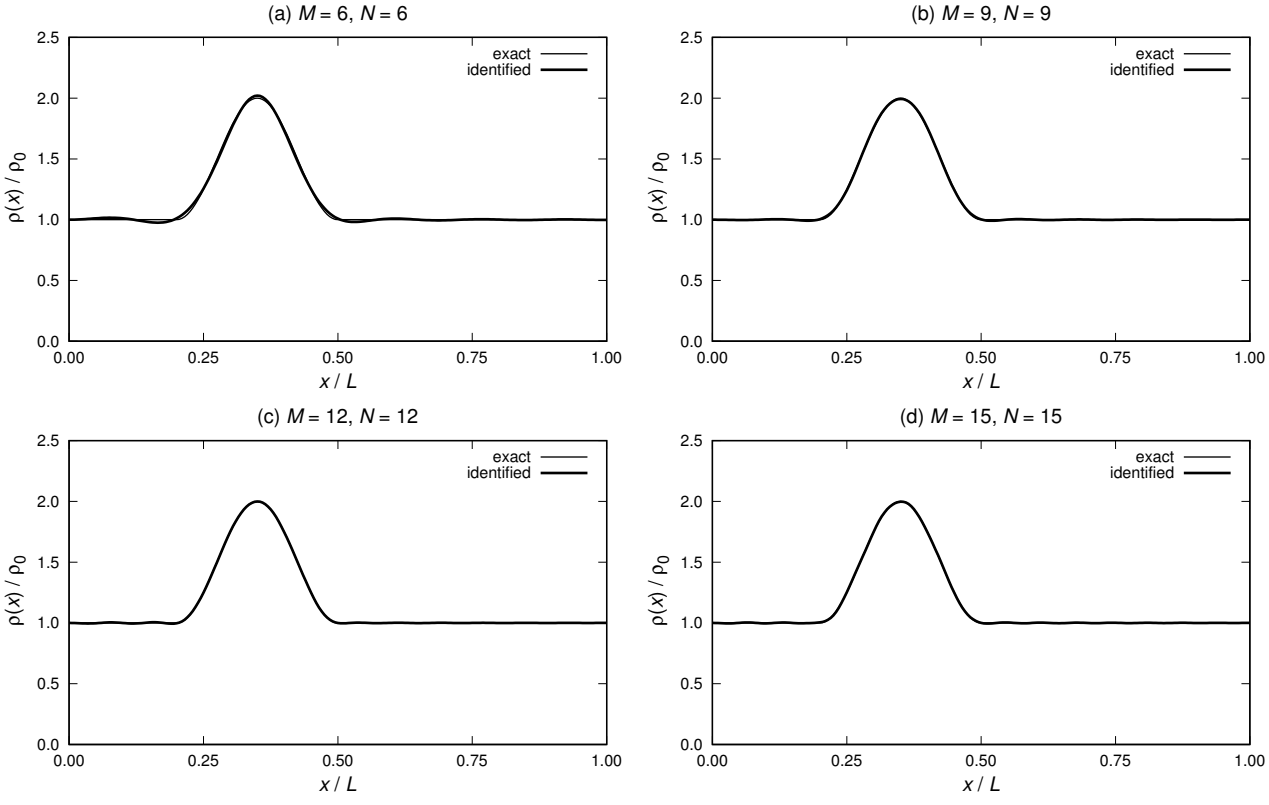

Figure 4: Reconstruction of smooth mass changes as in (38), with $\frac{s}{L} = 0.35$, $\frac{c}{L} = 0.30$, $t = 1.00$, using the first $N = M = 6, 9, 12, 15$ eigenfrequencies of both spectra.

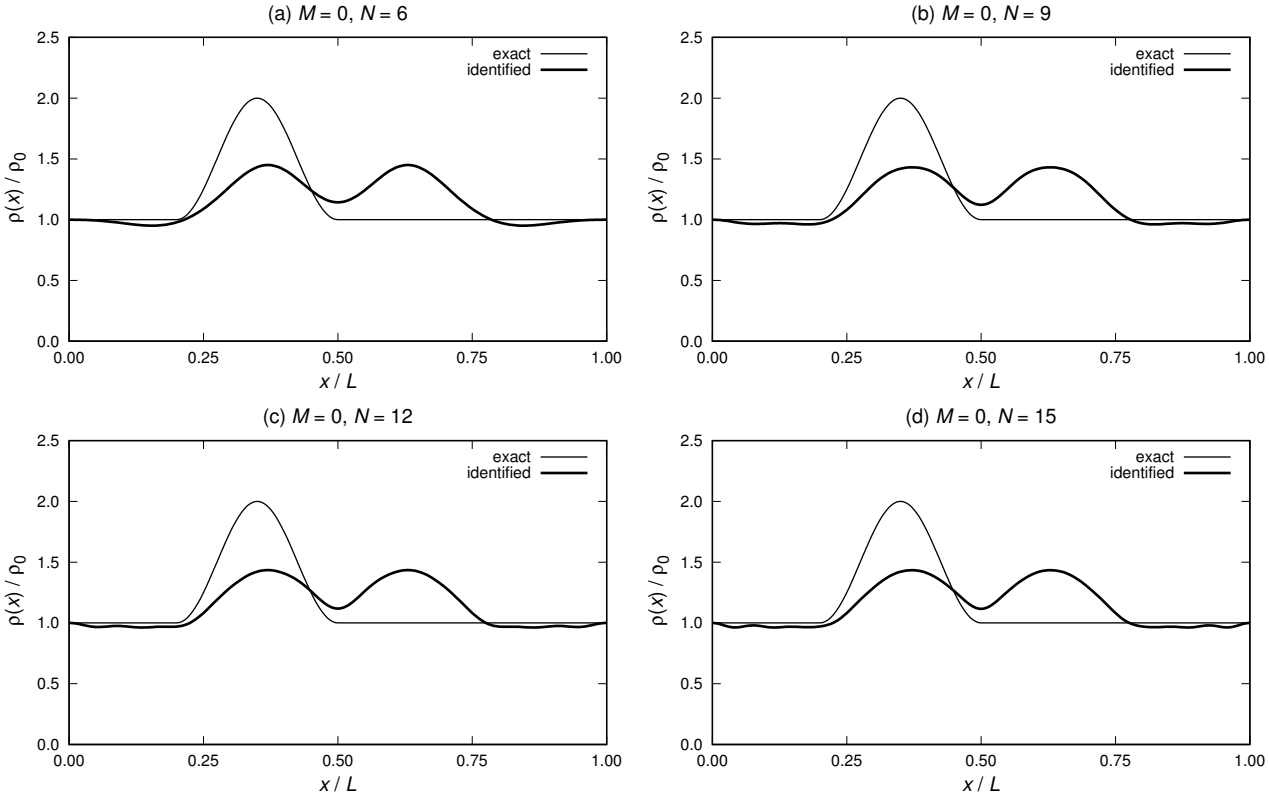

Figure 5: Reconstruction of smooth mass changes as in (38), with $\frac{s}{L} = 0.35$, $\frac{c}{L} = 0.30$, $t = 1.00$, using only the first $N = 6, 9, 12, 15$ eigenfrequencies of the clamped nanorod.

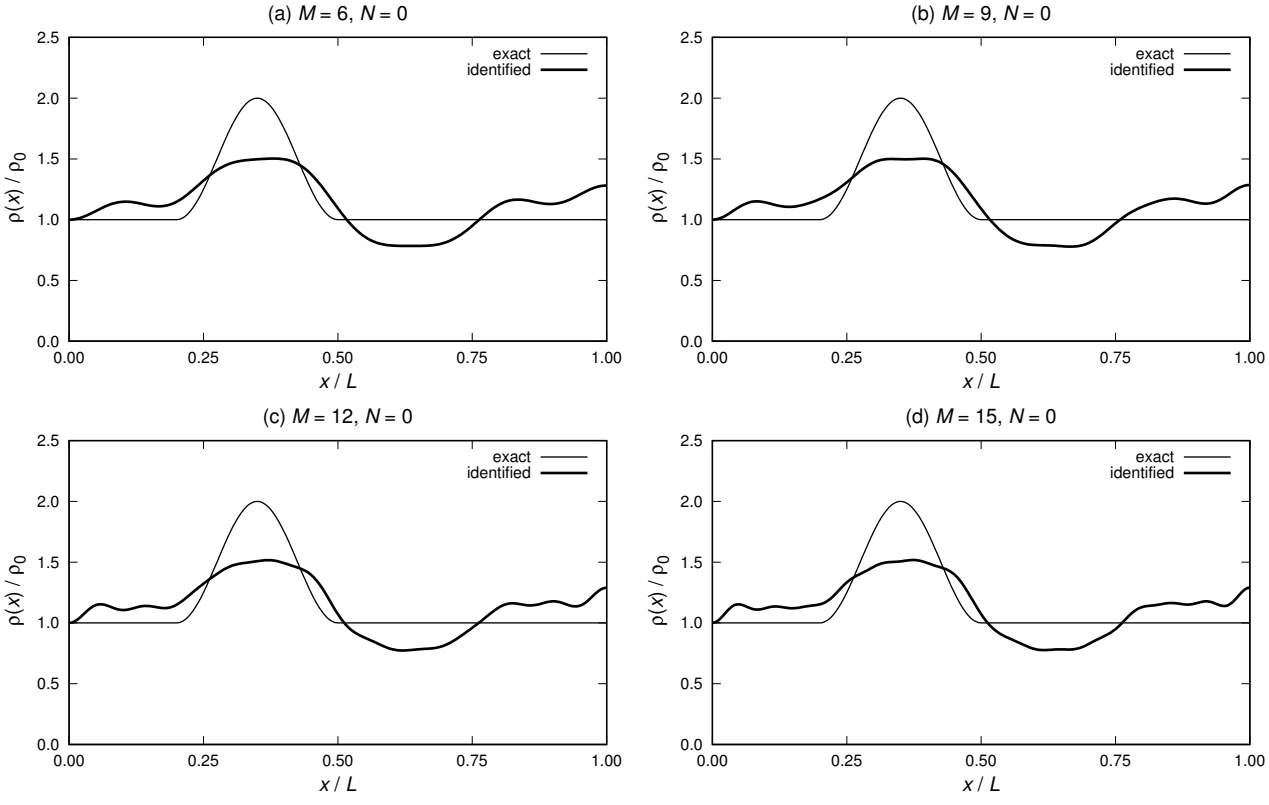

Figure 6: Reconstruction of smooth mass changes as in (38), with $\frac{s}{L} = 0.35$, $\frac{c}{L} = 0.30$, $t = 1.00$, using only the first $M = 6, 9, 12, 15$ eigenfrequencies of the clamped-free nanorod.

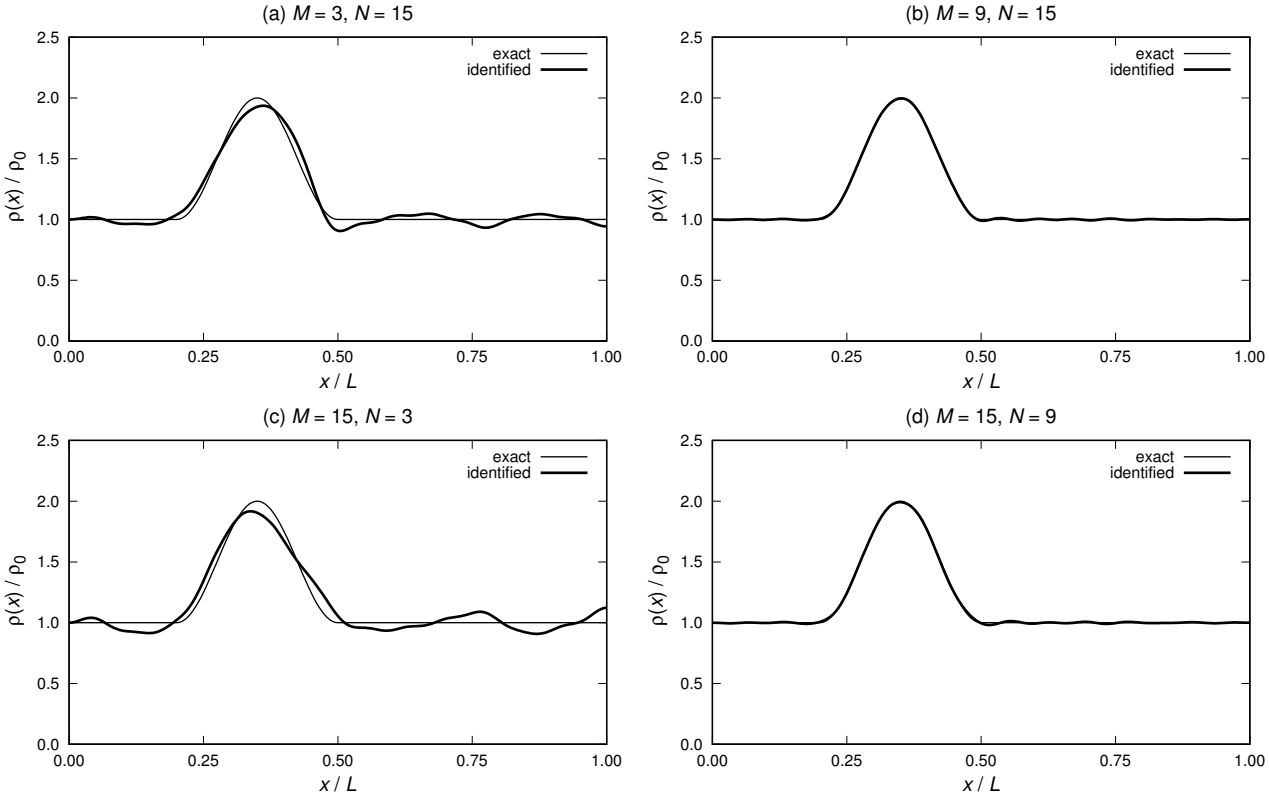

Figure 7: Reconstruction of smooth mass changes as in (38), with $\frac{s}{L} = 0.35$, $\frac{c}{L} = 0.30$, $t = 1.00$, using the first $(M, N) = (3, 15)$, $(M, N) = (9, 15)$, $(M, N) = (15, 3)$, $(M, N) = (15, 9)$ eigenfrequencies of the two spectra.

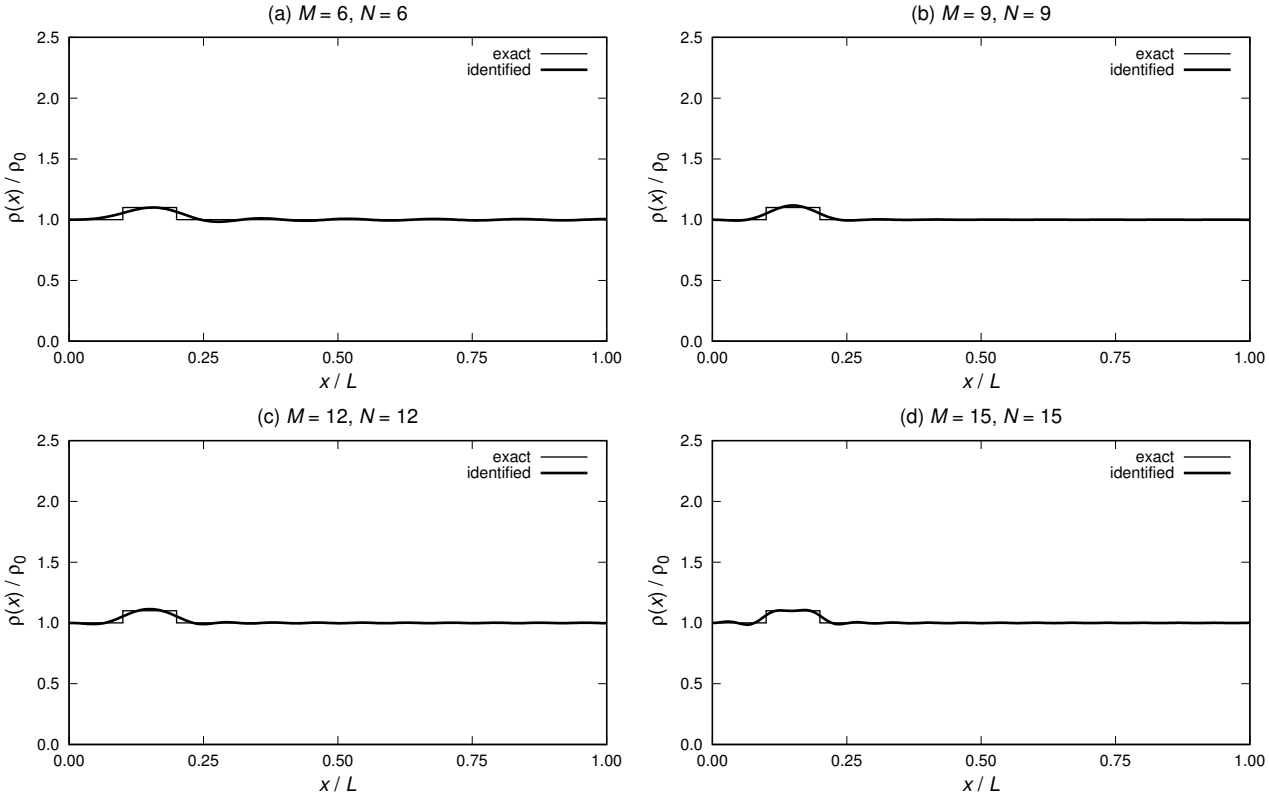

Figure 8: Reconstruction of discontinuous mass changes as in (39), with $\frac{s}{L} = 0.15$, $\frac{c}{L} = 0.10$, $t = 0.10$, using only the first $N = M = 6, 9, 12, 15$ eigenfrequencies of both spectra.

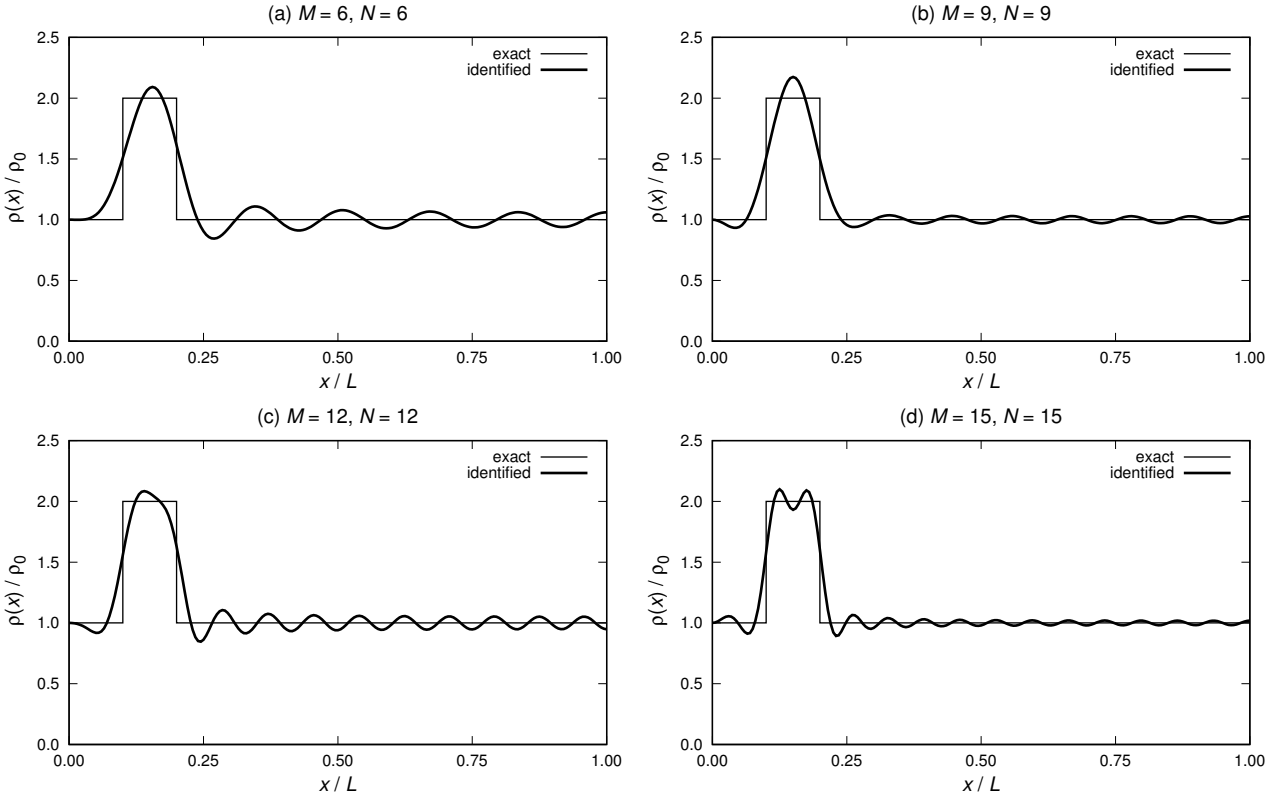

Figure 9: Reconstruction of discontinuous mass changes as in (39), with $\frac{s}{L} = 0.15$, $\frac{c}{L} = 0.10$, $t = 1.00$, using the first $N = M = 6, 9, 12, 15$ eigenfrequencies of both spectra.

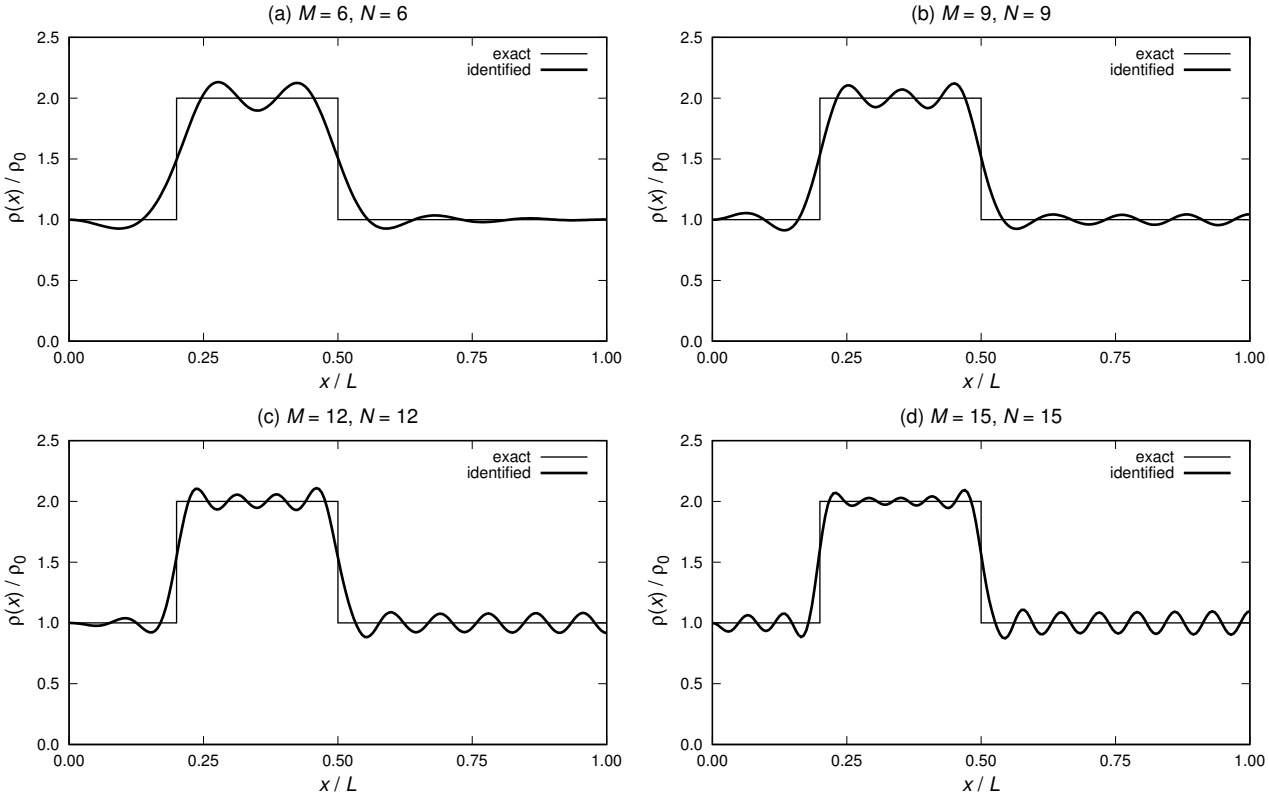

Figure 10: Reconstruction of discontinuous mass changes as in (39), with $\frac{s}{L} = 0.35$, $\frac{c}{L} = 0.30$, $t = 1.00$, using the first $N = M = 6, 9, 12, 15$ eigenfrequencies of both spectra.

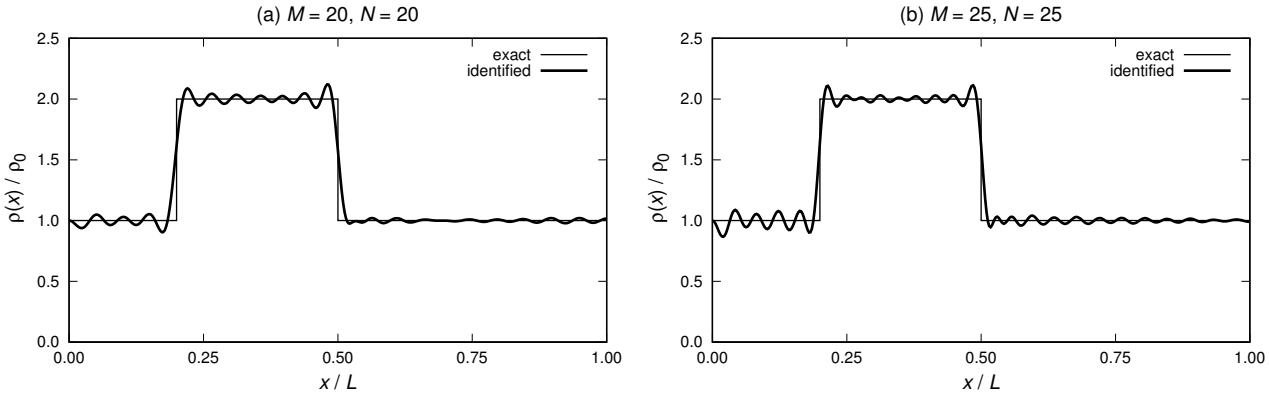

Figure 11: Reconstruction of discontinuous mass changes as in (39), with $\frac{s}{L} = 0.35$, $\frac{c}{L} = 0.30$, $t = 1.00$, using the first $N = M = 20, 25$ eigenfrequencies.

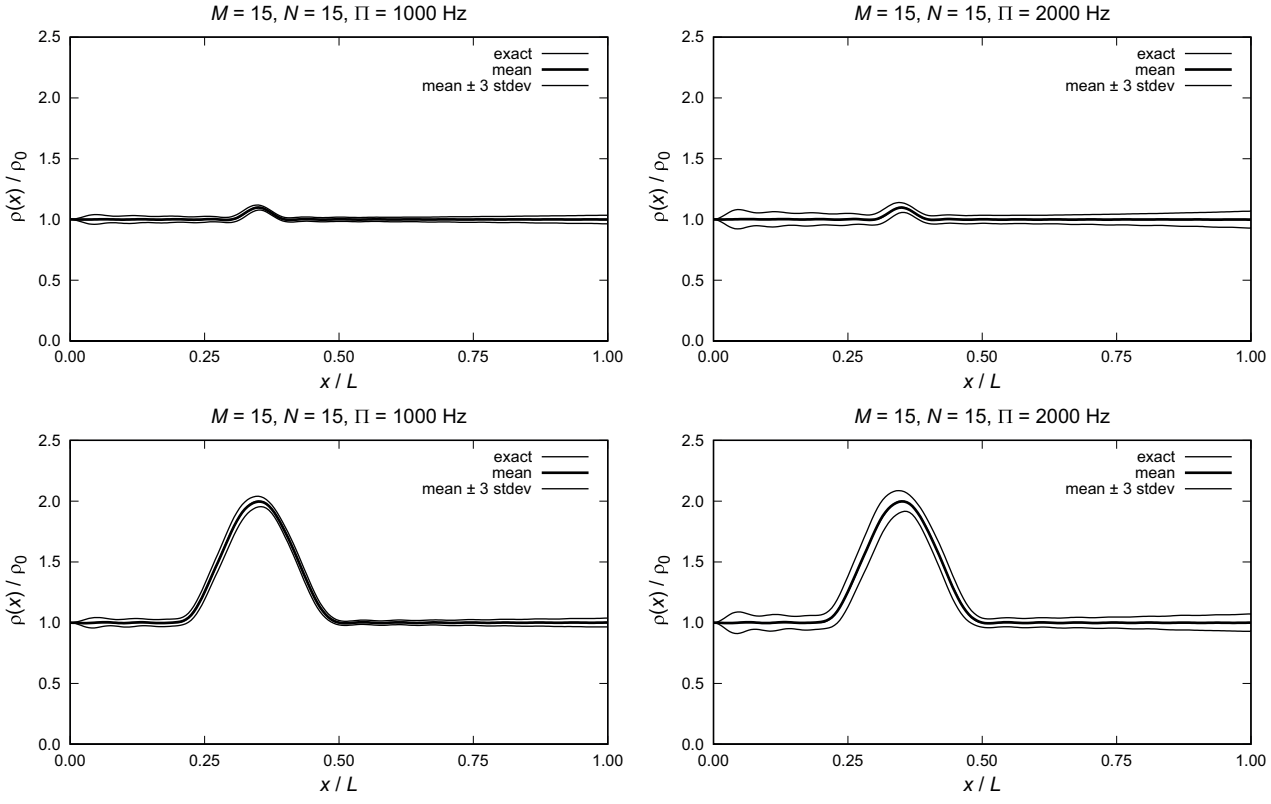

Figure 12: Noise effects on identification of smooth mass changes. Upper row: mass changes as in (38), with $\frac{s}{L} = 0.35$, $\frac{c}{L} = 0.10$, $t = 0.10$. Lower row: mass changes as in (38), with $\frac{s}{L} = 0.35$, $\frac{c}{L} = 0.30$, $t = 1.00$.

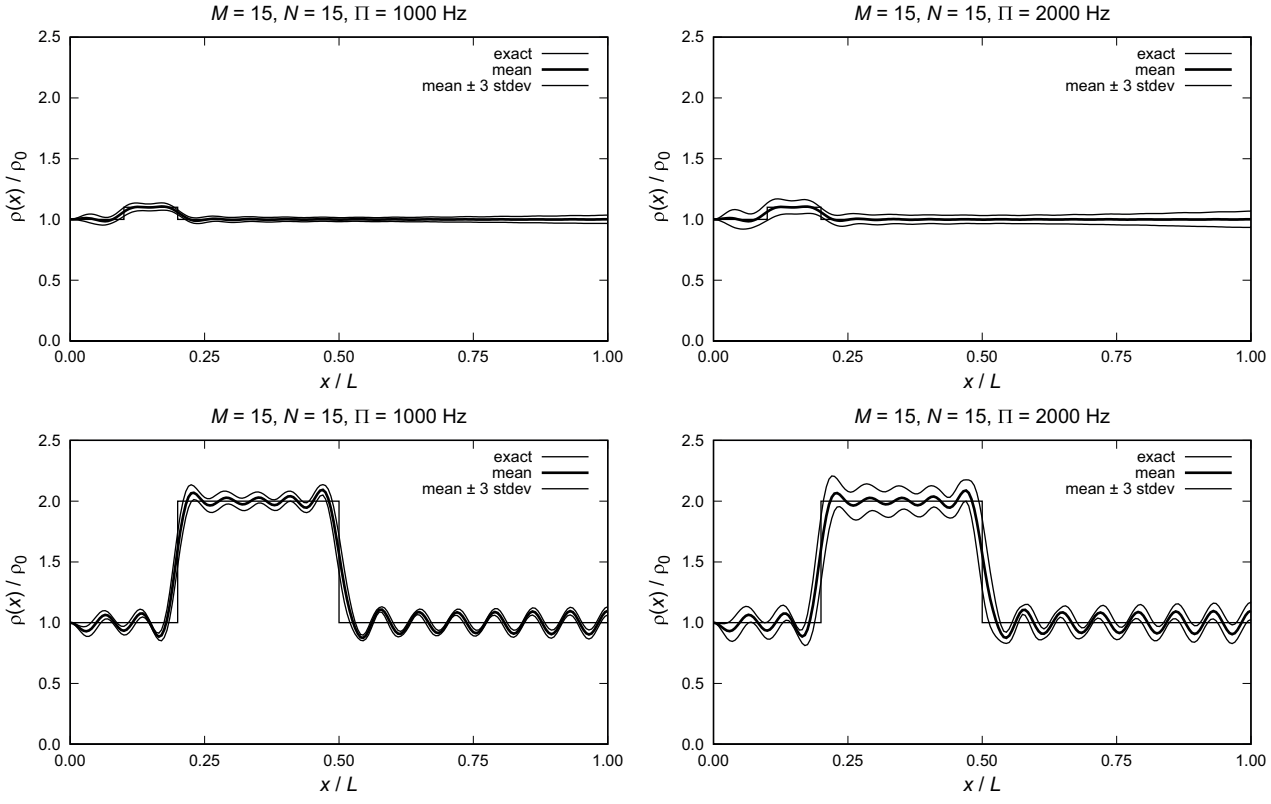

Figure 13: Noise effects on identification of discontinuous mass changes. Upper row: mass changes as in (39), with $\frac{s}{L} = 0.15$, $\frac{c}{L} = 0.10$, $t = 0.10$. Lower row: mass changes as in (39), with $\frac{s}{L} = 0.35$, $\frac{c}{L} = 0.30$, $t = 1.00$.